Development and application of Four-Wave Mixing and Cavity Ring-Down technique for spectroscopic studies

Inauguraldissertation

von

Achkasova Elena
aus Kamchatka (Russland)

Basel, 2007

Genehmigt von der Philosophisch-Naturwissenschaftlichen Fakultät

auf Antrag von

Prof. Dr. John P. Maier und Prof. Dr. Martin Jungen

Basel, den 26. Juni 2007

Prof. Dr. Hans-Peter Hauri

Dekan

To my parents

Acknowledgements

The completion of this thesis has ultimately been possible with the continued help and support of a number of people, and so to them I owe honest thanks.

Firstly, I am greatly indebted to Professor John P. Maier for enabling me to join his research group. His professional devotion, as well as his permanent and helpful suggestions enable successful finish of my thesis. I would like to extend my thanks also to Professor Martin Jungen for acting as the co-referee and Professor Hans-Peter Huber for being a part of mine examination board.

During my PhD I was honored to work with Dr. Mitsunori Araki, who introduced me not only the world of *ab initio* calculation and spectra assignment but also Japanese mentality through our numerous discussions. Furthermore thanks go to Dr. Alexey Denisov for his technical advice and assistance, for the fun times we had together.

Merci beaucoup à Dr. Fabio Mazzotti. Ca m'a fait très plaisir de travailler avec toi. Bon courage pour la suite.

Ich bedanke mich ganz herzlich bei Esther Stadler und Daniela Tischhauser für Ihre Geduld und die Hilfe den bürokratischen Sachen in Ordnung zu halten.

Herzlichen Dank an Frank Geringer. Die Fruchtbelieferung und unsere netten Plaudereien werde ich nie vergessen. Danke schön an Jacques, Ruth, Urs, Grischa, Dieter und Georg für die freundliche Atmosphäre im Institut. Unserer Werkstatt bin ich auch sehr dankbar für Ihre sorgfältige Arbeit.

My extraordinary thank goes to my colleague Ivan Shnitko for being ready to listen and help.

Schliesslich, einen liebesvollen Dank an Misch für deine Hilfe, Sorge und grosszügige Unterstützung während dieser 3,5 Jahren.

TABLE OF CONTENTS:

1 LINEAR AND NON-LINEAR SPECTROSCOPIC TECHNIQUES

1.1 INTRODUCTION

Optical diagnostic methods provide powerful tools for characterizing the molecular composition and detailed physical properties of molecular systems. The high intensity, coherent, and spectrally pure radiation provided by lasers, together with recent advances in laser spectroscopy, has revolutionized optical diagnostics. The unique properties of the laser techniques allow quantum state specific measurements to be performed with high temporal and spatial resolution. Applications of laser diagnostics are numerous and diverse, starting from fundamental spectroscopic measurements of isolated molecules in supersonic expansions, in combustion at high temperatures, to detecting complex macromolecules in biological systems. There is a variety of spectroscopic techniques available, each with its particular strengths and weaknesses that determine the area of their application. Important considerations for choosing a technique include sensitivity, applicability to a variety of chemical species, the capability for quantitative and qualitative measurements, and its experimental complexity.

1.2 LINEAR SPECTROSCOPY

In 1814, Josef Fraunhofer used a new and more precise apparatus to repeat an experiment performed by Newton more then a century before: he dispersed the solar spectrum into its component colors. The resolution of the Fraunhofer's spectroscope was greater than those used previously. Thus he found a new effect: narrow dark lines appeared in the solar spectrum with a define and unchanging pattern. Spectra of other light sources-particularly flames-showed similar structures often complemented with bright lines. When table salt was shaken into a dark flame, the bright orange light had exactly the same wavelength as two prominent dark lines in the solar spectrum.

Thus began spectroscopy. Within 50 years, certain dark and bright lines were identified as characteristic of the chemical elements. It was assumed that the energy in light could somehow excite the internal vibrations of atom, leading to absorption. Similarly, heat or electricity could excite vibrations which would radiate the energy away as light [1].

In 1864 Maxwell formulated the electromagnetic theory of light, in which he made the approximation that dielectric susceptibility and magnetic permeability are independent of the strengths of the applied fields, and thus the dielectric polarization and magnetization are linearly proportional to the field amplitudes,

$$\mathrm{P} = \overset{\Rightarrow}{\chi} \cdot \mathrm{E}; \tag{1.1}$$

$$\mathrm{M} = (\overset{\Rightarrow}{K} - \overset{\Rightarrow}{1}) \cdot \mathrm{H} \tag{1.2}$$

The resonant structure of the spectra were contained in the susceptibilities. Later one allowed the susceptibilities to be regarded as complex numbers and the optical frequency fields to be written in complex notations

$$\mathrm{E}(r,t) = \mathrm{Re}\, \mathrm{E}(r) \cdot e^{-i\omega t} = \frac{1}{2} \left\{ \mathrm{E}(r) \cdot e^{-i\omega t} + \mathrm{E}^*(r) \cdot e^{i\omega t} \right\}, \tag{1.3}$$

The wave equation thus became

$$\nabla^2 \mathrm{E} - \frac{1}{c^2} \frac{\partial^2}{\partial t^2} \mathrm{E} = \frac{4\pi}{c^2} \frac{\partial^2}{\partial t^2} \mathrm{P}, \tag{1.4}$$

which predicted a phase velocity in nonmagnetic media of

$$\upsilon = cn^{-1} = c\, \mathrm{Re}(1+4\pi\chi)^{-1/2}, \tag{1.5}$$

where n is the index of refraction. The attenuation in the absorbing media obeyed Beer-Lambert's law,

$$(\hat{k} \cdot \nabla) I = -2\kappa I, \tag{1.6}$$

where the unit vector $\hat{k}$ specifies the local direction of propagation, the amplitude attenuation constant κ

$$\kappa = \omega c^{-1} \, \text{Im}(1+4\pi\chi)^{-1/2},$$ (1.7)

and the observable intensity of the wave was related to the time vector as

$$I = \hat{k} \cdot \langle S \rangle = (nc/8\pi)|\text{E}(r)|^2.$$ (1.8)

The early workers in quantum mechanics recognized that variation of the index of refraction and attenuation coefficient contained crucial information as to the energy levels of the medium. Bohr related the attenuation coefficient to the probability of a transition between energy levels separated by the energy quantum of the light $E = \hbar\omega$. Fermi expressed the transition rate in terms of the matrix element of the dipole moment operator $\boldsymbol{\mu}$ = $e\mathbf{r}$ which connected the two levels

$$\Gamma_{ij} = \left(\frac{\pi}{2\hbar}\right)\left|\langle i|\mu \cdot \text{E}(r)|j\rangle\right|^2 \rho(E_i - E_j - \hbar\omega),$$ (1.9)

where the factor $\rho(E)$ is a density of states function that reflects the observed lineshape and e is the electronic charge. Actually, when the index of refraction of the medium is different from one, the dipole moment operator must be corrected for the local field and $\boldsymbol{\mu} \to ((n^2 + 2)/3)e\mathbf{r}$. Einstein calculated the probability for spontaneous light emission per unit time

$$A_{ba} = \frac{4n\left|\langle b|\mu|a\rangle^2\right|}{3\hbar^4 c^3}(E_b - E_a)^3$$ (1.10)

and pointed out that the transition rate in Equation (1.9) applies equally to absorption and stimulated emission processes. Kramers and Kronig [2] showed that the variation of the index of refraction was related to the absorption

$$\text{Re } \chi(\omega) = -\frac{1}{\pi} \int_{-\infty}^{\infty} \frac{\text{Im } \chi(\omega')}{\omega' - \omega} d\omega'; \qquad\qquad (1.11)$$

$$\text{Im } \chi(\omega) = -\frac{1}{\pi} \int_{-\infty}^{\infty} \frac{\text{Re } \chi(\omega')}{\omega' - \omega} d\omega'. \qquad\qquad (1.12)$$

Thus, the quantum mechanics of the classical tools of spectroscopy − emission, absorption, and dispersion − was well understood early in the twentieth century [3]. The fourth tool of linear spectroscopy - light scattering − requires more sophistication, and due to its irrelevance to this work will not be discussed.

1.2.1 Linear spectroscopic techniques

Among the leading linear techniques are spontaneous Raman scattering, laser-induced fluorescence (LIF), ionization spectroscopy, and cavity ring-down spectroscopy (CRDS). Absorption spectroscopy is widely used due to its overall applicability and conceptual simplicity. But quite often its practical utilization is restricted by the need to extract weak signals from large and fluctuating levels of baseline light. A number of different ingenious modifications which increase the absorption path length or use modulation schemes have been developed to improve the sensitivity of the absorption techniques. Alternatively, one can used other experimental methods which are induced by absorption of light, such as fluorescence in LIF, or ions in resonant enhances multiphoton ionization (REMPI). Unfortunately, because these techniques rely upon secondary interactions (fluorescence and ionization) certain limitations exist, as in LIF, where molecules that have unstable (dissociative or predissociative) excited electronic states are not detected.

1.2.1.1 Cavity ring-down spectroscopy

Cavity ring-down spectroscopy (CRDS) is a powerful direct absorption technique, which was developed by O'Keefe and Deacon [4] in 1988 for measuring the electronic

spectra of jet-cooled molecules and clusters with both high sensitivity and high spectral resolution. The method is based on measuring the decay rate of a pulse of light trapped in an optical cavity formed by a pair of highly reflective (R>99.9%) mirrors (see Figure 1.1).

$$\tau = \frac{d}{c(1 - R)}$$

$$\tau = \frac{d}{c(1 - R + \alpha l)}$$
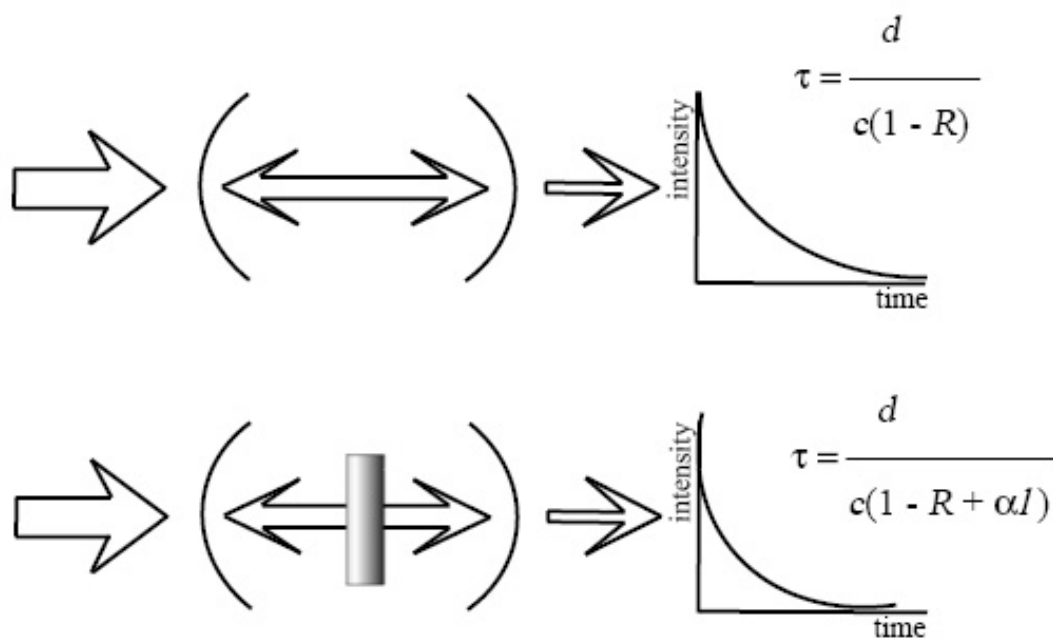
Figure 1.1. The principles of cavity ring-down spectroscopy.

The small amount of light that is trapped inside the cavity reflects back and forth between the two mirrors, with a small fraction (~1-R) transmitting through each mirror with each pass. The resultant transmission of the circulating light is monitored at the output mirror as a function of time and allows the decay time of the cavity to be determined. The intensity envelope of the discrete transmitted pulses exhibits a simple exponential decay. The time required for the cavity to decay to 1/e of the initial output pulse is called the "cavity ring-down" time. Determination of the ring-down time allows the absolute single pass transmission coefficient of the cavity to be determined with high accuracy, given the mirror spacing. The apparatus is converted to a sensitive absorbing spectrometer simply by

replacing an absorbing medium between the two mirrors and recording the frequency dependent ring-down time of the cavity, which is determined by

$$\tau(\nu) = \frac{d}{c(1 - R + \alpha(\nu)l)} \quad , \tag{1.13}$$

where d is the optical length of the cavity, c the speed of light, R the averaged reflectivity of the two mirrors and αl the absorbance for a sample present in the cavity with absorption coefficient α and length l. As was already mentioned, the ring-down time reflects the rate of absorption rather than the magnitude of the absorption, and as such it has important advantages compared with conventional absorption techniques: the method is immune to pulse-to-pulse fluctuations in the laser power and the very long absorption pathlengths that are obtained by confining the light pulse several microseconds in the cavity make this technique ideal to study unstable species.

The minimum absorbance measured with the CRDS apparatus is limited by the mirror reflectivity R and the minimum change in the time τ that can be detected. For mirror reflectivity as high as R=99.99% and for the reported accuracy in the ring-down time determination of $(\Delta\tau/\tau)_{min} = 5*10^{-3} - 2*10^{-3}$ [5, 6] the minimum measured absorbance $(\alpha l)_{min}$ is on the order of a few parts in 10^{-7}.

1.3 NONLINEAR SPECTROSCOPY

Before the development of the laser, the interactions investigated between optical frequency fields and matter were weak enough that linear theories sufficed. A more general treatment was developed in the 1930s when strong coherent source of radio-frequency and microwave radiation became available.

Detailed understanding of nonlinear resonance phenomena began with the discovery and explanation of nuclear magnetic resonance in the late 1940s. The dynamics of most of the interesting nonlinear optical resonance is analogous to that of an ensemble of spin ½ systems.

More generally, the phenomena observed in the steady state can be described by a dielectric polarization density expanded as a power series in the electric field,

13

$$P_\alpha = \chi_{\alpha\beta}E_\beta + \chi_{\alpha\beta\gamma}{}^{(2)}E_\beta E_\gamma + \chi_{\alpha\beta\gamma\delta}{}^{(3)}E_\beta E_\gamma E_\delta + ...,\qquad(1.14)$$

where the subscripts denote Cartesian coordinates. The complex tensor coefficients of the higher-order terms are called nonlinear susceptibilities [7]. The nonlinear optical effects useful in spectroscopy – saturated absorption, stimulated Raman gain, four-wave mixing, multiquantum absorption, etc. - result from these terms. Techniques based on these effects extend the range of optical spectroscopy and increase its applicability and precision. Thus, for example, Doppler broadening can be eliminated; weak and forbidden processes can be enhanced by orders of magnitude. New information on the energy levels, lifetimes, collisional processes, coupling strengths, etc can be obtained by analysing the resonant behaviour of the nonlinear susceptibilities.

1.3.1 Degenerate four-wave mixing

1.3.1.1   Introduction

During the past several years a relatively mature nonlinear technique, degenerate four-wave mixing (DFWM), has received renewed attention because of its potential role as an optical diagnostic. In the DFWM experiment three incident beams are used which have identical (degenerate) frequency ω but are distinguishable due to having their directional and/or polarization characteristics. Nonlinear interactions with the target molecules give rise to a fourth output beam, with energy conservation demanding that the frequency of this coherently "scattered" radiation be equal to ω. The direction of propagation and polarization of the emerging signal wave also obey various conservation criteria.

The availability of four-wave mixing as a probe of molecular structure comes from frequency-dependent variations in the efficiency of the signal production. In particular, these changes in optical response reflect fundamental properties of the molecules of interest (e.g. transition energies, decay rates), with exceptionally strong DFWM interactions expected to accompany resonant excitation of allowed molecular transitions. Thus by monitoring the intensity of the output radiation as a function of the incident frequency ω an

essentially background-free, "absorption-like" spectrum can be measured for the species of interest. Because the four-wave mixing process does not rely upon "secondary process" (like fluorescence or ionization) to identify the location of a transition, such techniques can be applied to any system that shows resonant attenuation or amplification of light.

1.3.1.2 *General principles*

In the gas phase DFWM is a hybrid between LIF and Coherent Anti-Stokes Raman Scattering (CARS). Similarly to CARS the signal is detected as a spatially and temporally coherent beam, but like LIF the technique relies on the resonant interaction. It is therefore more sensitive than non-resonant CARS and is less complicated experimentally.

Four-wave mixing techniques rely on the interaction of three-coherent light beams to induce a non-linear polarization in a medium through the third-order term in the susceptibility, $\chi^{(3)}$. The induced polarization then generates a fourth coherent beam. In DFWM the three input beams have the same frequency ω, and so the polarization and the generated beam also oscillate at ω. In a dilute molecular medium (*e.g.* gas) the mixing process is enhanced by many orders of magnitude whenever the frequency is resonant with a molecular transition. Thus a spectrum can be obtained by observing the intensity in the signal beam as a function of ω.

At present no generalized theory of DFWM including collisional, polarization, and saturation effects exists. The most complete description to date is the work of the group at Sandia National Laboratory, Livermore [8-10] and publications of the group at Yale University, New Haven, Connecticut [11, 12].

1.3.1.3   Superposition of two laser beams

The experimental arrangement for the production of laser-induced grating is conceptually simple although its realization is sometimes quite demanding. The basic setup is shown on Figure 1.2 [13]
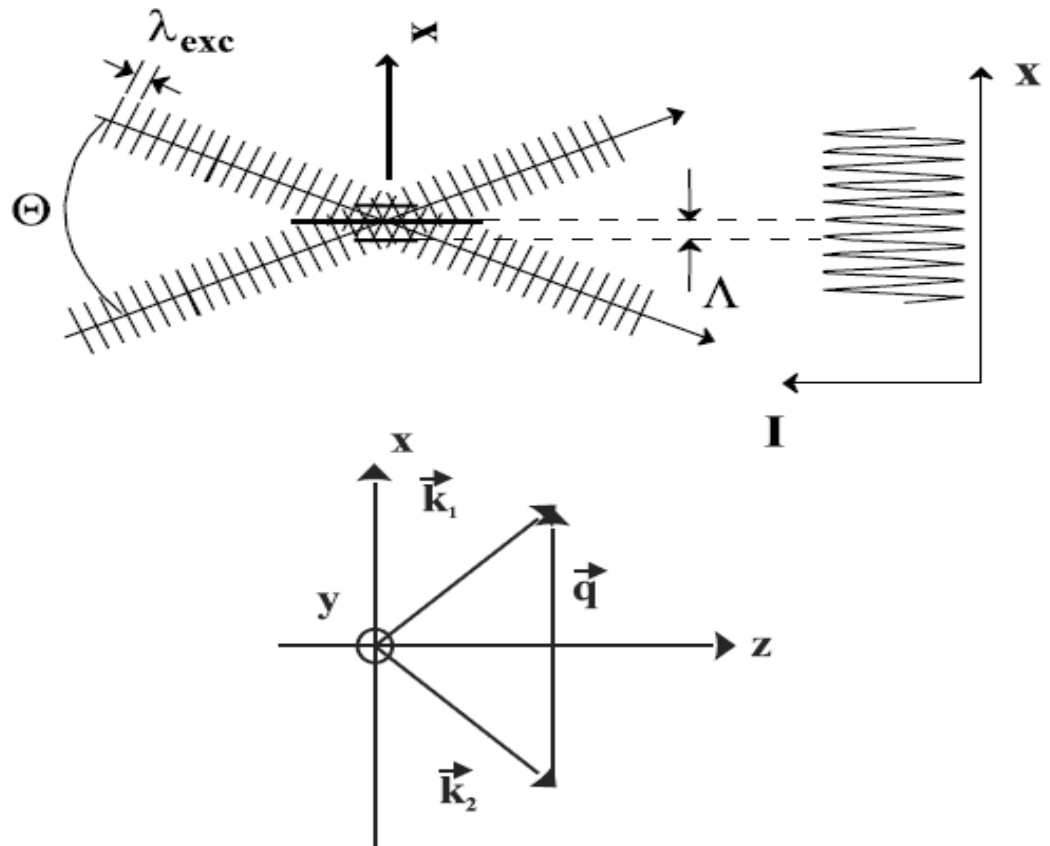
Figure 1.2. Grating formation by interference of two light beams with wavelength λ_{exc} and wave vectors k_1 and k_2.

The two laser beams, in the following called pump beams, with wave vector k_1 and k_2 and electric field amplitude E_1 and E_2, intersect at the angle θ in the medium. Their superposition generates an interference pattern characterized by the grating vector **q**

$$\mathbf{q} = \pm (\mathbf{k}_2 - \mathbf{k}_1) \qquad\qquad (1.15)$$

The absolute value of the grating vector, $q = |\mathbf{q}|$, is related to the fringe spacing of the interference pattern according to

$$q = \frac{2\pi}{\Lambda}$$
(1.16)

where

$$\Lambda = \frac{\lambda_{exc}}{2\sin\frac{\theta}{2}}$$
(1.17)

Here λ_{exc} denotes the wavelength of the excitation laser. Λ is also called the "grating wavelength". The total electric-field amplitude distribution E(r, t) inside the interference region is the sum of the electric field amplitudes of the two pump beams. The pump beams are assumed to be plane waves. If they have a finite cross section the lateral extent of the interference region is limited. A calculation of this effect is given in [14] and [15].

1.3.1.4   Optical gratings

Laser-induced grating are formed in a medium by various resonant and non-resonant mechanisms as a response to the spatially modulated light field that arises from the interference of two pump beams. The total electric field produces some material excitation, which then leads to a change of the optical properties. More precisely, the material excitation couples to the refractive index n and to the absorption coefficient α which then exhibit a grating like modulation with amplitude Δn (λ_{pr}) and $\Delta\alpha$ (λ_{pr}), respectively [13]. Both amplitudes are functions of the probing wavelength λ_{pr}. Such a laser-induced grating can be probed by detecting the diffracted light from a third laser beam, which can have a frequency different from the one of the pump beams. The part of the probe beam which has been diffracted by the grating is called the signal beam. Gratings characterized by a large grating thickness compared to the fringe spacing are called thick gratings (see Figure1.3). The Fourier transform spectrum of a thick grating is dominated by two well defined peaks along $\pm\mathbf{q}$ with negligible contributions in other directions. Therefore, thick gratings can be efficiently probed only if the Bragg condition is obeyed,

$\mathbf{k}_{pr} - \mathbf{k}_s = m\mathbf{q}$, m = ±1, 2, …
(1.18)

where $\mathbf{k}_{pr}$ and $\mathbf{k}_s$ are the wave vectors of the probe and signal beams, respectively. On the contrary, the Fourier transform spectrum of a thin grating is not an isolated spike along one direction, say x, but contains contributions along a direction orthogonal to x of the order of d^{-1} caused by the finite thickness of the sample.
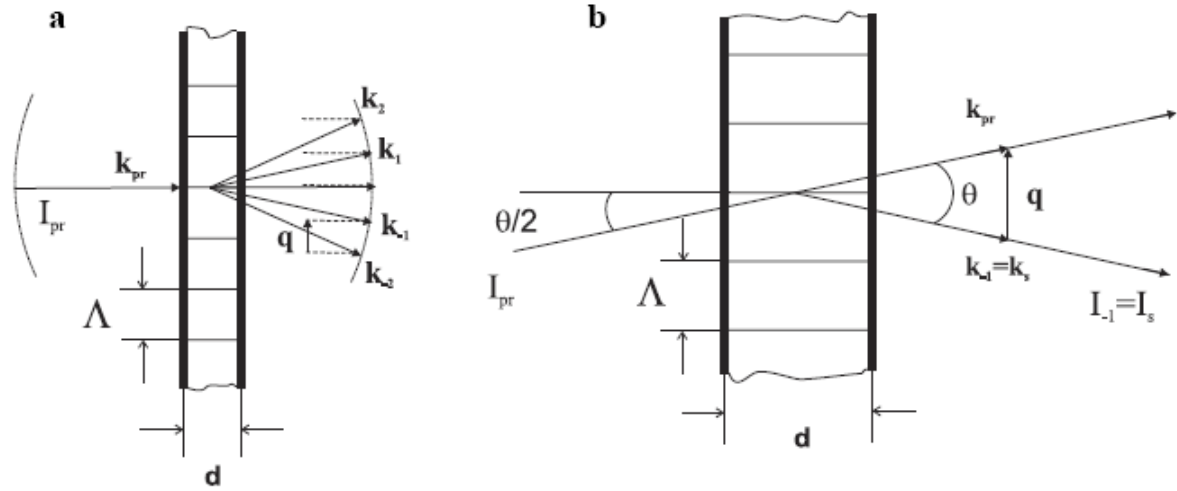
Figure 1.3. Scheme of diffraction at (a) a thin and (b) a thick grating, where d is the grating thickness and Λ the grating specing.

Therefore, constructive interference is possible at arbitrary directions of the probing beam [13]. For the experiments described in this work only thick gratings and their first-order diffraction, i.e. m = ±1 will be considered. One can see from Figure 1.4 that the Bragg condition given in Equation (1.18) determines both the direction of the wave vector $\mathbf{k}_{pr}$ and its absolute value, which is equal to the absolute value of $\mathbf{k}_s$.

Figure 1.4. Vector relation of the highly symmetric arrangement of excitation beams, probe and (the first order) diffracted signal beam for the diffraction at a thick grating.

The amplitude of the probe wave diffracted into the first order from an optical grating is to a first approximation equal to the modulation a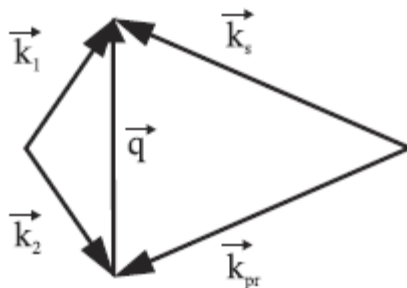mplitude $\Delta\mathbf{n}$ of the complex refractive index $\mathbf{n} = n + i\alpha/2k_{pr}$, where n is refractive index, α is the absorption coefficient and k_{pr} is the length of the wave vector of the light for which the optical properties are measured.

For ideal plane-wave interaction, characterized by a spatially constant intensity transverse to the beam direction and thus spatially constant grating amplitudes, the normalized intensity of the first-order ($m = \pm 1$) diffracted beam I_s/I_{pr} is [13]

$$\frac{I_s}{I_{pr}} = \eta = \left| \frac{\pi \Delta \mathbf{n} d}{\lambda_{pr}} \right|^2 = \left(\frac{\pi \Lambda n d}{\lambda_{pr}} \right)^2 + \left(\frac{\Delta \alpha d}{4} \right)^2, \qquad (1.19)$$

where I_s and I_{pr} are the intensities of signal beam and probe beam, respectively.

Equation (1.19) for the diffraction efficiency η of a laser-induced grating is valid for grating with sufficiently small $|\Delta n|$ and low absorption in the medium, i.e. $\alpha d \ll 1$. For beams of finite width the intensities in Equation (1.19) can be replaced by the respective ratio of the light fluxes. Very small refraction index changes Δn and the optical path changes $\Delta n d$ can be measured by diffraction. For example, a diffraction efficiency of much less than 10^{-5} can be easily detected, corresponding to an optical path length change $|\Delta n d| \approx \lambda/1000$. The phase is thus measured with interferometric sensitivity.

1.3.1.5   Experimental configurations

Several DFWM configurations exist. Figure1.5 schematically illustrates the so-called "phase-conjugate" experimental configuration, which is widely use in spectroscopic studies due to its relatively easy implementation and sub-Doppler frequency response [12]. In this geometry, two pump waves, having electric field vectors $\mathbf{E}_f$ and $\mathbf{E}_b$ (subscripts denoting "forward-going" and "backward-going") are directed through a molecular sample in a coaxial and counterpropagating manner. A probe beam, with electric vector $\mathbf{E}_p$, crosses the pump fields under a small angle θ forming the interaction region for the DFWM process. These three input beams are coupled through a non-linear medium giving rise to a

signal wave $\mathbf{E}_s$, which is emerges in a direction that is exactly collinear and counterpropagating to the probe beam. The signal beam generated in this manner satisfies phase-matching or momentum conservation criteria for all angles θ with the wavevectors being related

$$\mathbf{k}_s = \mathbf{k}_f - \mathbf{k}_p + \mathbf{k}_b = - \mathbf{k}_p \qquad\qquad (1.20)$$

where the latter follows from the fact that $\mathbf{k}_b = - \mathbf{k}_f$ for the phase-conjugate geometry. In a similar manner, the frequency of the signal wave follows from the energy conservation criteria:

$$\omega_s = \omega_f - \omega_p + \omega_b \qquad\qquad (1.21)$$

Because the input beams have the same frequency ω, $\omega_s = \omega$.
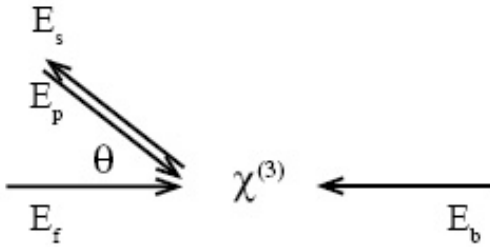

Figure 1.5. The "phase-conjugate" configuration for DFWM spectroscopy. Two pump beams ($\mathbf{E}_f$ and $\mathbf{E}_b$) are directed through the molecular sample in a coaxial and counterpropagating manner while the third incident probe beam ($\mathbf{E}_p$) intersects them under a small angle, θ. The signal beam ($\mathbf{E}_s$) emerges collinear with the probe radiation.

The main disadvantage of this configuration is the need to indroduce appropriate optical elements (e.g. beamsplitter) or some other discriminatory mechanism (e.g. polarization) in order to extract the desired signal radiation, which retraces the path passed by the incident probe wave. The residual light scattered from these optical elements is a major source of the baseline in the properly aligned and optimized DFWM apparatus.

There are two "boxes", known also as "boxcars" [16], variants of DFWM which eliminate the source of such incoherently scattered background light without having to insert any collection optics into the path of the incident radiation. In Figure1.6 a forward-box and a backward-box geometries are shown. Thus three incident waves are directed through a molecular sample along distinct diagonals of a rectangular parallelepiped (or box). Nonlinear interactions within the target medium produce a fourth signal beam, which

emerges along the "dark" axis of detection defined by the remaining diagonal [17, 18]. Both of these nonplanar schemes enable the direct detection of the output wave.

Analogous to phase-conjugated geometry the signal beam satisfies a phase-matching and energy conservation criteria.
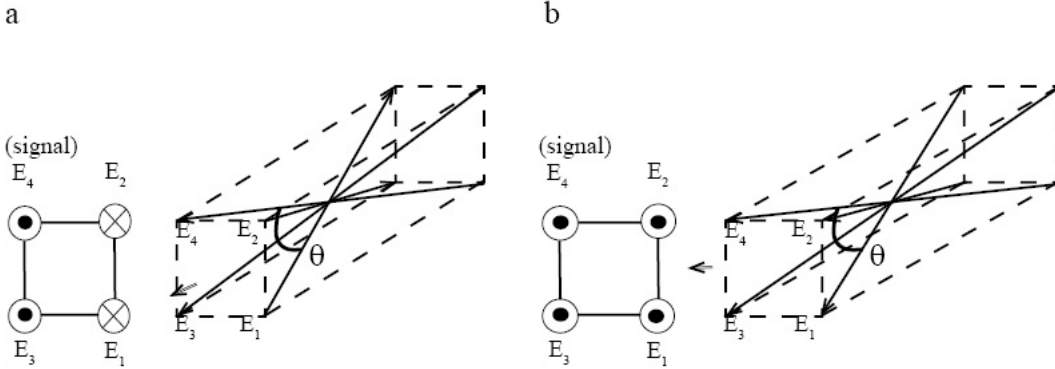

Figure 1.6. "Box" configurations for DFWM spectroscopy. Three incident waves of identical frequency are directed through a molecular medium along distinct diagonals of a rectangular parallelepiped (or box). Nonlinear interaction gives rise to a fourth signal beam. (a) illustrates the backward-box geometry; (b) illustrates the forward-box geometry.

Because no additional beamsplitters or other devices are used to extract the fourth beam, the forward-box and backward-box configurations lead to an efficient increase of signal strength due to the fact that in such configurations all signal protons are collected and an overall decrease in baseline noise occurs due to minimal scattering of light from the optical components [17]. However the box schemes, compared with the phase-conjugated geometry, require more sophisticated alignment of the detection optics. The path of $\mathbf{E}_s$ is not collinear to any incident radiations (viz., $\mathbf{k}_s \neq -\mathbf{k}_2$). Thus one must create "artificial signals" for alignment. In this work a thin cell (1mm) containing dye solution was inserted into the DFWM interaction region. The absorption in this condensed media gives rise to strong four-wave mixing processes with generation of the signal beam which has sufficient intensity and is visible.

1.3.1.6   *Signal intensity and saturation effects*

The simplest analytical model for DFWM in the absorbing media of a two-level system was established by Abrams and Lind [19, 20], and has been successfully applied to molecular spectroscopy [9, 21]. This model assumes negligible absorption of the two pumps beams and allows small absorptions of both the probe (I_{pr}) and signal (I_s) beams. Assuming monochtomatic fields with equal pump beam intensity I and under the condition $I_{pr} \ll I$ and $I_s \ll I$, the integrated signal intensity in the limit of small absorption ($\alpha_0 L < 1$) is given by [9]

$$I_s^{int} = \frac{3\pi}{2T_2} \frac{1}{1+\delta^2} \alpha_0^2 L^2 \frac{4\left(\frac{I}{I_{sat}^0}\right)^2}{\left(1+4\frac{I}{I_{sat}^0}\right)^{5/2}} I_{pr} \qquad (1.22)$$

where L is the interaction length and α_0 is the unperturbed line-center absorption coefficient given by

$$\alpha_0 = \frac{\omega T_2}{2c\hbar\varepsilon_0} \mu_{eg}^2 \Delta N_{eg}. \qquad (1.23)$$

ΔN_{eg} is the population difference in the absence of electromagnetic fields, μ_{eg} the dipole moment. I_{sat}^0 is the saturation intensity at the line center ($\delta = 0$)

$$I_{sat} = \frac{\varepsilon_0 c\hbar}{2T_1 T_2 \mu_{eg}^2}(1+\delta^2) \qquad (1.24)$$

where T_1 and T_2 are the longitudinal (population) and transversal (coherence) relaxation times. In particular, I_{sat}^0 provides a measure of the field strength for which the optically-induced oscillation of population between ground and excited states of a rovibronic transition becomes comparable to the rates of the relaxation/dephasing processes. In order to provide a powerful tool for spectroscopic measurements, the dependence of the DFWM

23

signal strength upon the experimental parameters, for example incident light intensities and molecular properties (transition dipole moment and decay rates) must be understood. Some insight into the behavior of the four-wave mixing processes comes from consideration of the absorber model in the limits of low and high pump intensity (i.e. measured relative to I_s^0). Thus, using Equation (1.22)

$$I << I_{sat}^0; \quad I_s^0 \propto \frac{\alpha_0^2}{T_2} \left(\frac{I}{I_{sat}^0} \right)^2 I_{pr} \propto \mu_{eg}^8 T_1^2 T_2^3 I^3 \Delta N_{eg}^2, \tag{1.25}$$

$$I >> I_{sat}^0; \quad I_s^0 \propto \frac{\alpha_0^2}{T_2} \sqrt{\frac{I}{I_{sat}^0}} I_{pr} \propto \mu_{eg}^3 \sqrt{\frac{T_2}{T_1}} \sqrt{I} \Delta N_{eg}^2, \tag{1.26}$$

Since in most DFWM experiments pump and probe beams have the same source of optical radiation, it is useful to consider the case when $I_p = I$. Under this condition, and for $I << I_{sat}^0$, the signal intensity cubically depends on the incident intensity. The high-power limit for I_s^0 shows a behavior which is independent of both I and I_p. This suggests a possible advantage for working in the saturated regime since the laser fluctuations will not influence the output signal.

Furthermore, I_s^0 attains the highest value when $I = I_{sat}^0 / 2$ yielding

$$I_s^0 \propto \frac{\alpha_0^2}{T_2} I_{pr} \propto \mu_{eg}^2 T_2 I \Delta N_{eg}^2. \tag{1.27}$$

Detailed analysis of the Abrams and Lind theory confirms this maximization of DFWM response at near-saturation intensities.

The asymptotic expressions for I_s^0 show significant differences in their dependence on transition dipole moment matrix element, μ_{eg}. Thus, the low intensity regime is characterized by the $|\mu_{eg}|^8$. The four-wave mixing response at high intensities is found to be proportional to $|\mu_{eg}|^3$. Farrow et al. [9] have investigated the dependence on the transition dipole moment of isolated line intensities in the NO A $^2\Sigma^+$ − X $^2\Pi$ (0, 0) band. The effects of finite laser bandwidth were taken into account by comparing theoretical and

experimental intensities that have been spectrally integrated. Their observations are in reasonable agreement with the simple two-level model described above and predict the same limiting dependences.

1.3.1.7   *Applications*

In 1986 Ewart, et al reported the use of DFWM as a mean of monitoring OH radicals produced in combustion environments [21]. Although DFWM experiments were originally performed mainly in atomic vapors, this pioneering work on OH stimulated much of the current interest in four-wave mixing spectroscopy. There is ongoing research towards understanding fundamental and practical limitations of this technique. The OH radical still remains the most studied of any molecular system [22-24], however there is a number of other diatomic molecules, including both stable (NO [17, 18, 25-27], CO [28-30], I_2 [31-36], H_2 [29, 30, 37], and O_2 [29, 30]) and transient (NH [22], C_2 [38], CH [38, 39], SH [40], and NaH [41, 42]) species which have been successfully studied using DFWM. The quantitative analysis of trace amounts in atmospheric and combustion related processes has been the primary motivation for many of these efforts. However the potential spectroscopic applications of degenerate four-wave mixing have not stayed unnoticed. For example, two-photon resonant schemes relying upon DFWM detection have permitted exploration of high-lying (one-photon forbidden) electronic states in both atomic and molecular systems.

While polyatomic molecules, with their more varied internal degrees of freedom, present additional difficulties for any spectroscopic probe, resonant DFWM measurements have been performed on a number of systems such as HCO [43, 44], NO_2 [45-48], H_2O [29, 30, 49], SiC_2 [50, 51], NH_3 [52], C_3 [50, 51], CH_3 [53], CS_2 [54], SO_2, S_2O, H_2CO [55, 56], glyoxal [57], benzene [58], and pyrazine. Moreover, non-fluorescing species like azulene, malonaldehyde [59], as well as weakly-bound molecular complexes (e.g., glyoxal dimmer [57]) have been investigated by means of DFWM.

The availability of tunable infrared sources has made possible the investigation of molecules in their ground state. For example, high resolution infrared DFWM experiments have been done on C_2H_2 [60, 61], NO_2 [62], and CH_4 [60].

A limitation of DFWM is its sensitivity. According Equation (1.22), the DFWM signal is proportional to the second order of the total number of absorbing species and the absorption light path. Thus, the DFWM method is ideally suited to use together with the slit nozzle approach. Vaccaro's group performed the DFWM spectroscopy on carbon disulfide (CS_2) [63] in a pulsed slit-jet expansion. The slit length of ≈ 1 cm gained two orders of magnitude of signal intensity when compared with a previously used 0.5 mm diameter round nozzle.

The group of W. Kong reported high quality DFWM spectra of pyridazine [64], which they could observe only by using a slit nozzle. Their efforts to record the pyridazine spectra using a 1-mm-circle nozzle were unsuccessful.

The double-resonance technique of TC-LIGS, which will be presented in the following chapter, has an analogous $(Nl)^2$ dependence and thus is also capable of exploiting the benefits afforded by the slit-jet conditions.

Also non-resonant schemes of DFWM have been widely used in the time-domain form. The recent extension of resonant-enhance DFWM techniques into picosecond and femtosecond regimes should encourage new research fields directed at understanding the nature of unimolecular and biomolecular chemical transformations.

1.3.2 Two-color four-wave mixing (laser-induced grating) spectroscopy

In this chapter two-color resonant four-wave mixing (TC-RFWM) will be discussed in detail. It has been applied to a variety of spectroscopic problems, including investigations of molecular structure and dynamics in regimes of extreme vibrational excitation.

1.3.2.1 Introduction

Two-color resonant four-wave mixing (TC-RFWM) describes another set of fully resonant wave mixing processes in which two optical fields have frequencies in resonance with two distinct molecular transitions. Such two color experiments provide a useful tool

for detecting optical transitions from rovibronically excited molecules, particularly when more well known methods such as REMPI and LIF are inappropriate, for example, when an intermediate state is predissociative. The experiment is most conveniently set up in the forward-box geometry [65].

Signal generation in RFWM can be interpreted as the formation of and diffraction from laser-induced gratings. Thus, the TC-RFWM method is known as two-color laser-induced grating spectroscopy (TC-LIGS)[49].

TC-RFWM was first demonstrated on the 32-0 P(51) and 34-0 P(102) rovibrational transitions in the B $^3\Pi_{0u}^+ \leftarrow$ X $^1\Sigma_g^+$ absorption band of I_2 [49]. These lines are pumped by the output of a frequency-doubled Nd: YAG laser. Two equal intensity beams (the pump beams) generated from this laser were focused together into a sample cell containing ca 300 m Torr of I_2 to form a laser-induced grating. Output from the Nd: YAG pumped dye laser (the probe beam) was also focused into the cell in order to overlap the pump beams spatially. By scanning the dye laser in the required region two types of signals have been observed. The first corresponds to the case when the laser frequency matches that required to stimulate emission into the rotational level of the $v=5$ vibrational manifold in the $^1\Sigma_g^+$ state. In this case the signal is produced by scattering off the population grating produced in the $J = 50$ and $J = 101$ levels in $^3\Pi_{0u}^+$ state. However, another signal can be generated, which arises because the optical pumping also creates a "depletion" grating in the rovibrational levels of the ground states, which diffracts the probe beam whenever its frequency is resonant with a transition from one of these levels. Thus, by using non-degenerate beams information about levels in both electronic states can be obtained.

TC-RFWM can be used for investigating of highly vibrationally excited molecules. Butenhoff and Rohlfing [45] applied this technique to study the predissociation spectroscopy of NO_2 in a molecular beam. In their experiments, the pump beam was tuned through the dissociation threshold while the probe laser was fixed to a well characterized absorption line below the dissociation limit. Therefore, the signal beam was generated by diffraction of the ground-state depletion grating whenever the pump laser frequency matched a transition out of the rotational level selected by the probe laser. As the pump laser frequency is tuned the LIGS spectrum represents the square of the absorption spectrum from the level selected by the probe laser. An important issue is that although the excited-state grating vanishes on a very short timescale as a result of photodissociation (few ps in this case), the signal originates from the long-lived ground state depletion

grating. Thus, one of the major applications of this type of spectroscopy is to study non-fluorescent molecules.

An advantage of studying LIGS in the collision-free environment of a molecular beam is that other effects which tend to complicate the interpretation of the spectrum can be eliminated [65].

1.3.2.2 *Phase matching considerations in two-color LIGS*

Two-color LIGS, like any four-wave mixing process, obeys the energy and phase matching criteria. The energy conservation criterion means that the signal beam and the probe beam have identical frequency, *i.e.* $\omega_s = (\omega_1 - \omega_1) + \omega_2$. The phase matching condition is given by the vector sum: $\mathbf{k}_1 + \mathbf{k}_2 = \mathbf{k}_1' + \mathbf{k}_s$, where the wave vector magnitudes are $k_i = 2\pi/\lambda_i$ the two grating beams are denoted by $\mathbf{k}_1$ and $\mathbf{k}_1'$ ($k_1 = k_1'$), and $k_s = k_2$. In spectroscopic measurement the grating and probe-beam angles are fixed and either λ_1 or λ_2 are scanned. Exact matching occurs for only one combination of grating and probe frequencies; at other frequency combinations there will be a phase mismatch that reduces the intensity of the signal beam. Thus unlike DFWM, which is phase matched at all frequencies, these effects of the phase mismatch must be considered in the TC-LIG experiments.
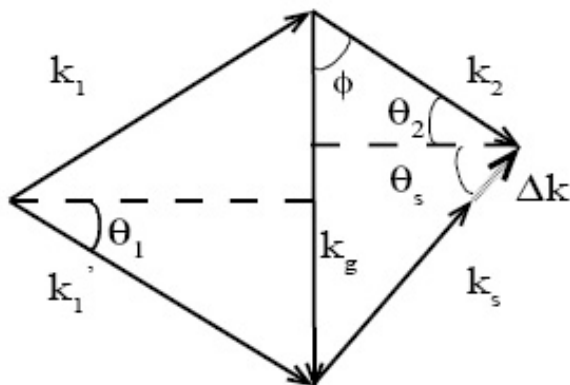

Figure 1.7. The wave vector scheme for two-color LIGS in the forward-box geometry for the case in which the probe frequency lies below the phase matched value. k_1 and k_1' are wave vectors of grating beams, k_2 is a probe beam, k_s is a signal wave, and k_g is a wave vector of the grating. Δk defines the phase mismatch.

For a wavevector mismatch of $\Delta \mathbf{k} = (\mathbf{k}_1 - \mathbf{k}_1' + \mathbf{k}_2) - \mathbf{k}_s$, a straightforward analysis shows that the TC-LIGS response behaves proportion to $\sin^2 (\Delta kl/2)/ (\Delta kl/2)^2$, where $\Delta k = |\Delta \mathbf{k}|$ and l is the interaction length. However, one can avoid the restrictions placed by the momentum conservation by sensible selection of the experimental configuration, with the widest frequency range for "approximate" phase-matching obtained when the incident beams of varying frequency copropagate.

Butenhoff and Rohlfing have considered this problem assuming that the signal wave emerges in a direction which minimizes the value of Δk [45]. For a planar geometry in with the grating-forming beams remain fixed at $\omega_1 = \omega_2$ while the frequency of the nearly copropagating probe wave ω_3 is scanned, the effective phase-match bandwidth $\Delta\omega$, defined as the Full-Width at Half-Maximum (FWHM) height for the central segment of the $\sin^2 (\Delta kl/2)/ (\Delta kl/2)^2$ function, has the form:

$$\Delta \omega \propto \frac{(\omega_3 / \omega_1)^2}{l \sin^2 (\theta_{21} / 2)} \qquad (1.28)$$

where θ_{21} is the angle between two grating-forming beams [12]. The predicted inverse proportion between the phase-matching bandwidth and the interaction length l is consistent with relaxation of the Bragg scattering condition expected to accompany contraction of the grating. Butenhoff and Rohlfing confirmed the validity of the equation (1.28) through their experimental measurements in methanol dye solution [45]. The phase-matching bandwidths for small crossing angles and short path lengths are sufficiently large, *i.e.*, several hundred to a few thousand cm^{-1}, that signal loss due to phase mismatch does not limit the tuning range in TC-LIGS [45].

2 SUPERSONIC JET METHOD AND ITS APPLICATIONS IN SPECTROSCOPY

Molecular spectroscopy deals with absorption or emission of electromagnetic radiation. It is well known that spectroscopy is one of the most powerful tools for characterization, identification and further analysis of molecules. Doppler effects and molecular interactions can lead to broadened profile in emission and absorption spectra. As a result, there is need to measure the spectra of isolated molecules, free from the external interactions and cooled in order to simplify structure and reduce Doppler broadening. For studying molecular dynamics in lower energy vibrations (particularly conformational transitions), high resolution (< 1 cm^{-1}) is usually required.

UV-VIS radiation is required for studying the electronic states of molecules. It should be emphasized that in electronic spectroscopy lines are more susceptible to Doppler broadening and molecular interactions than in IR spectroscopy. Using gaseous samples is a one way of overcoming these problems; however, this approach can only be employed for compounds with relatively high vapor pressures otherwise, condensation still occurs.

Molecular interactions in the condensed phase at low temperatures can be reduced by using matrix isolation. By condensing the vapour of the studies molecules together with an excess of neutral carrier gas (usually argon or neon), individual molecules are separated and their mutual interactions are significantly reduced. This method is useful particularly in reducing hydrogen bond and dipole interactions, however, van der Waals interactions of molecules with the carrier gas are still observed.

Supersonic jets are frequently used to obtain sharpened spectra. An adiabatic expansion (pressure p_0 and temperature T_0) into vacuum converts internal energy of the carrier gas vapour into its kinetic energy. This sharpens the Maxwell-Boltzman distribution in the velocity of the molecules and their translational cooling to temperature T. The cooling of large molecules in the supersonic jet is effective when the diameter of the nozzle is relatively large with respect to the free path of the molecules.

Because chaotic thermal motions of molecules are replaced by linear motion in one direction, one can say that translational degrees of freedom are cooled.
Here, the parameters of state for an ideal gas expanding under adiabatic conditions are given by the equation:

$$\frac{T}{T_0} = \left(\frac{p}{p_0}\right)^{\frac{\kappa-1}{\kappa}} = \left(\frac{\rho}{\rho_0}\right)^{\kappa-1} = \left[1 + \frac{(\kappa-1)M^2}{2}\right]^{-1} \qquad (2.1)$$

where:

M - the Mach number,

T_0 - the initial temperature in the nozzle (considered as the translational temperature of the carrier   gas),

p_0 - the initial pressure of gas in the nozzle,

ρ_0 - the initial density of gas in the nozzle,

κ - c_p / c_v (c_p, c_v - heat capacities at constant pressure and constant volume, respectively).

T, p, ρ, and M are the parameters at a given point of the jet.

As a consequence of collisions between the molecules and the atoms of the carrier gas the former transfer their rotational and vibrational energy to the latter.

However, the supersonic jet lacks thermodynamical equilibrium among its translational, rotational, and vibrational degrees of freedom. Relaxing vibrational states is relatively slow; it requires many collisions which gradually decreases as the expansion grows. Thus, vibrational cooling is less effective. One should note that the populations of levels is determinated by the kinetics of the cooling process, and may therefore not follow a Maxwell-Boltzman distribution. Temperatures obtained in the jet are comparable to those obtained by cryogenic methods (i.e. ~ 0.05-2 K for translation, ~ 0.2-10 K for rotation, and 20-40 K for vibration).

One of the important parameters describing the expansion process is the so called Mach number (M): the ratio of the jet velocity to the speed of sound at a given point. Because the speed of sound decreases as the degree of expansion increases, Mach values can reach on the order of 100. This is why gas flowing out of the jet is described as supersonic. Because the supersonic jet is considered a continuous medium, the Mach number is given by the following equation:

$$M = A\left(\frac{X}{D}\right)^{\kappa-1} \qquad (2.2)$$

where:

A - the constant (dependent on *D* and κ). For monatomic gases it is equal 3.26.

X - the distance from the nozzle,

D - the diameter of the nozzle,

κ - c_p / c_v

  Another important feature is a shock wave forming around the supersonic jet during the expansion. When the appropriate pressure of the gas surrounding the jet is maintained, this wave is dense enough to make the jet effectively isolated. Therefore, measurements should be made in the so called "silence zone", which is isolated from the rest of the chamber by the shock wave and Mach disk.

The area covered by the silence zone is described by the equation:

$$x_m = 0.67D\sqrt{\frac{P_0}{P_1}} \tag{2.3}$$

where x_m is the distance between the nozzle and the Mach disk. The region available for spectroscopic purposes within the isentropic expansion core typically starts around 5-10 nozzle diameters downstream from the nozzle and extends to the Mach disk. For example, for an expansion of 1000 Torr into a chamber of 0.1 Torr out of a nozzle of 0.1-mm diameter, one expects to find the Mach disk 6.7 mm downstream. Thus, a 5-mm long region, extending between 1 and 6 mm downstream from the nozzle is available.

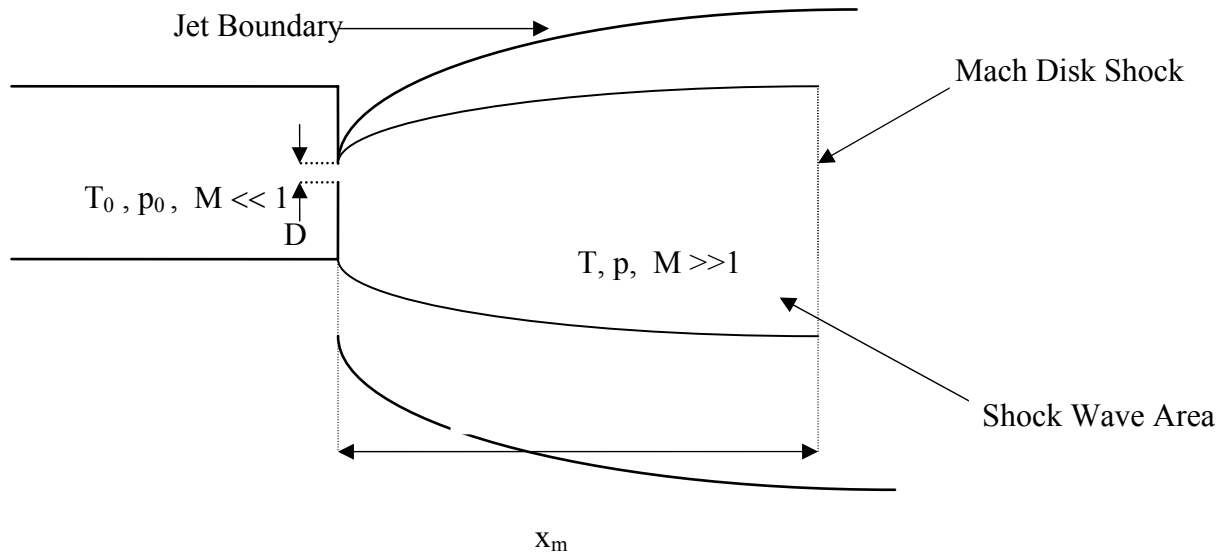 The geometry of the supersonic jet is shown in Figure 2.1.

Figure 2.1. The supersonic jet cross-section.

By using a pulsating jet instead of continuous flow, a smaller amount of gas can be introduced into the chamber, allowing lower sample consumption and higher sensitivity using lasers synchronized with the pulsed nozzle. The frequency of the nozzle opening varies from several to several hundred times per second. The opening time of the nozzle is on the order of 100 μs.

Supersonic jets have found widespread application in many branches of spectroscopy. Applied together with laser techniques, it is a very powerful method for studying a variety of exotic species, with particular success in the high resolution spectroscopic investigations of radicals and molecular ions.

3 EXPERIMENTAL SETUP

In the both experiments the radicals of interest have been produced in a pulsed discharge slit nozzle using acetylene or allene as a precursor. The slit nozzle is mounted on a two-dimensional translation stage so that the distance between the slit and the probe laser beam can be varied from 0 – 11mm to allow precise overlap between the gas flow and laser beam(s). The plasma source is placed into a stainless-steel cross piece, evacuated by a roots blower system with a total pumping capacity of 2775 m^3/h, which maintains a 10^{-2} mbar background pressure. While running the plasma the pressure in the chamber can be varied from ~0.08 to ~0.15 mbar.

The pulsed multihole slit nozzle source incorporating a discharge in a high pressure expansion consists of two stainless-steal electrodes, which are separated by insulators. The first electrode is pulsed with high negative voltage of -250 – 1000V (using a Velonex 345-F HV power supply) while the second electrode is grounded. The dimension of the slit is 30mm*300μm. Both insulators and metal parts are mounted to the body of the nozzle with electrically isolated screws. The scheme of the slit source is shown in Figure 3.1.
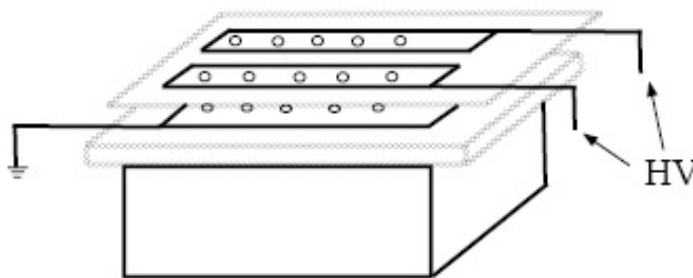

Figure 3.1. The scheme of the slit nozzle source.

3.1 CAVITY RING-DOWN EXPERIMENT

The high finesse optical cavity, which consists of two dielectric-coated mirrors, is the most sophisticated part of the CRDS experiments. The mirrors are connected with flexible bellows to opposite sides of the cross piece, defining the 52 cm cavity. Thus, a stable optical resonator with a spacing of longitudinal modes of $0.008cm^{-1}$ is formed from 7.75 mm diameter mirrors having a 1000 mm radius of the curvature. Hence using a laser with a bandwidth of $0.05\ cm^{-1}$ a multimodal cavity excitation was always allowed, reducing side interference effects in the cavity. The mirrors are aligned by adjusting high precision threaded screws. Two tilted quartz windows were fixed outside the cavity and seal the chamber. In order to protect the mirrors against contaminants a stream of helium is injected into the mirror holder forming "helium curtains". The mirrors used in this work were manufactured by Research Electro Optics Inc, Boulder, Colorado USA. The reflectivity coefficient of the mirrors, depending on wavelength, was approximately 99.98-99.998%.
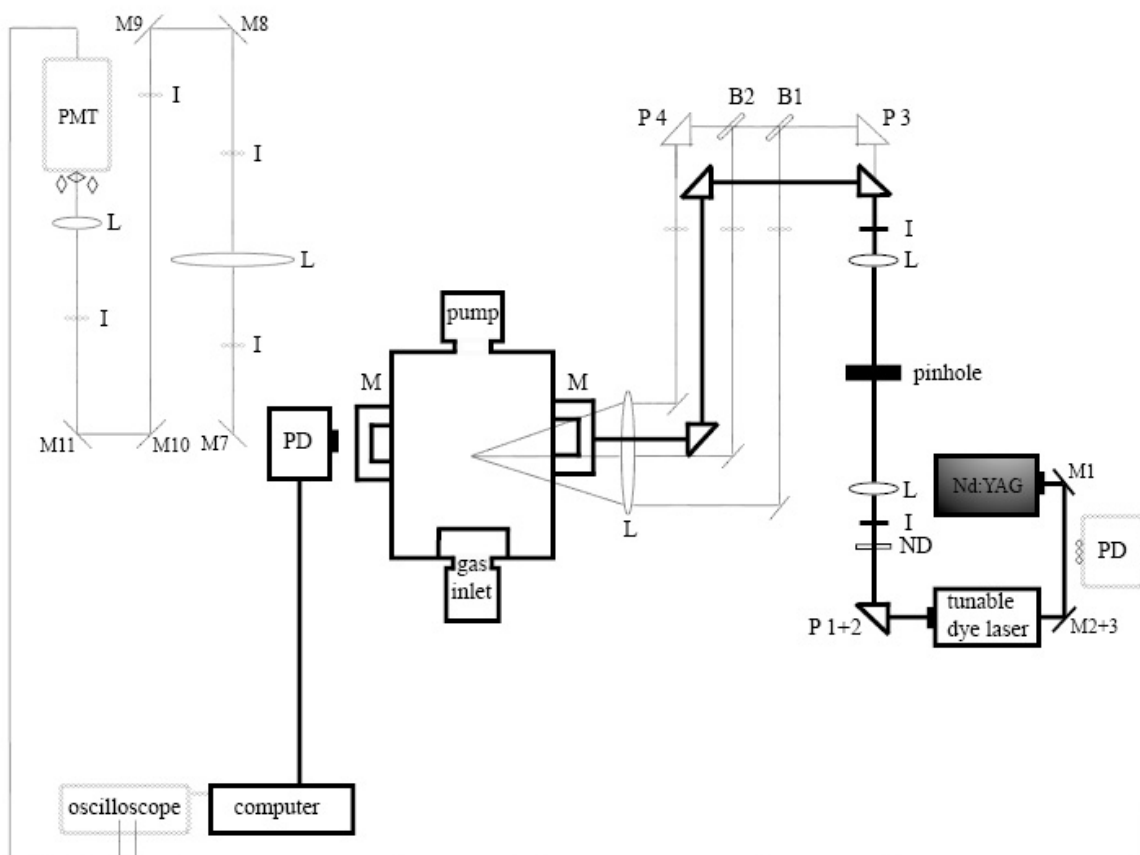
Figure 3.2. Schematic diagram of the experimental configuration used for performing CRDS measurements. The abbreviations used in here are defined as follows: M-mirror, L-lens, I-iris, P-prism, B-beamsplitter, PMT-photomultiplier tube.

As a source of monochromatic light an eximer pumped dye laser system was used. The dye laser was pumped by a 308 nm XeCl eximer laser at 60 Hz (COMPEX 110 manufactured by Lambda Physik). The average energy of the pulse was about 120 mJ. The tunable light was generated using a SCANmate 2E dye laser Lambda Physik (340-900) nm. The linewidth of the dye laser was about 0.1-0.15 cm^{-1} and could be reduced to 0.06 cm^{-1} by introducing an intracavity etalon. The laser radiation was focused into the optical cavity and spatially filtered by means of a 1:1 telescope equipped with a 100 μm pinhole. Because the gas valve runs at 30 Hz, background absorption could be subtracted from every plasma pulse.

The light leaking out of the cavity was detected by a broad band photodiode (Hamamatsu S1336 – 44BQ, 190 – 1100 nm). To block the background light and the light generated by the discharge narrow-band optical filters are placed in front of photodiode.

The amplified signal was displayed on a 300 MHz 8-bit digital oscilloscope (LeGroy 9310). Two gates, one set at the beginning and the other at 2-3 τ of the decay curve, were used to determine the exponential waveform. A third time gate is used for background subtraction. The typical ring-down time varied from 30 to 50 μm. Spectra were calibrated using the Burleigh pulsed wavemeter WA-4500 (400 to 1100 nm) with wavelength determination accuracy of 0.02 cm^{-1}.
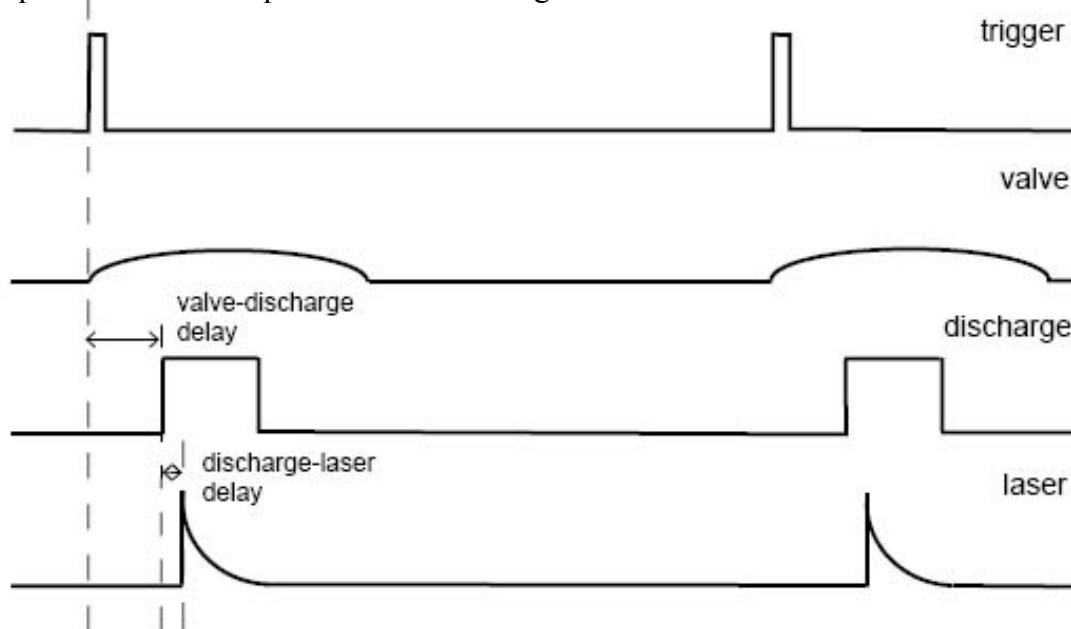
The experimental time sequence is shown in Figure 3.3.

Figure 3.3. The time scheme of the running experiment (at 20 Hz).

3.2 DEGENERATE FOUR-WAVE MIXING EXPERIMENT

The experimental configuration included a dye laser (SCANmate 2E, Lambda Physik) pumped by the third harmonic of Nd:YAG laser (Innolas Splitlight 600) pulsed at 20 Hz with 8 ns pulse duration. Coumarin 307 was used allowing continuous coverage of the 485-550 nm spectral range. The fundamental bandwidth of this radiation source was 0.15 cm^{-1} and could be reduced to 0.06 cm^{-1} by means of intracavity etalon. The dye laser produced average pulses of 1 mJ. The output laser beam was directed through a Keplerian telescope with a 100 μm diameter pinhole in the middle, where it was spatially filtered and recollimated to a near-Gaussian beam with final 0.3 mm diameter. Two Pellicle beamsplitters were used to produce the three nearly equivalent input waves. A set of broadband dielectric mirrors and quartz prisms established the forward-box configuration,

viz. the three beams were directed along the major diagonals of a rectangular parallelepiped with the ~2° crossing angle between adjacent wave vectors leading to an interaction region (defined by the volume of mutual beam overlap) of roughly 2 cm length. Because the length of the slit is 3 cm the interaction area is determined by the geometry of the beams. A set of neutral density filters inserted into the path of the incident beam reduced its initial pulse energy to a few μJ to avoid the signal saturation. A quartz convex lens with focal length 1000 mm was used to focus the three radiation waves (with a diameter 0.3 mm) in the middle of the experimental chamber ~ 5 mm downstream from the slit nozzle. Careful alignment of the three input beams was performed by positioning a 25 μm pinhole in the middle of the chamber before setting up the ion source. The signal beam was generated in the medium according to phase-matching conditions and propagated along the "dark" axis of detection defined by the remaining major diagonal. It was re-collimated by means of the second lens (f = 1000 mm) and allowed to travel ~4 m thought a number of irises, optical and spatial filters to remove the scattered radiation and light spikes from the discharge. The signal was directed to a short-focal-length lens (f = 20 mm) that focused the beam through a pinhole (50 μm) on a photomultiplier tube (Hamamatsu H 3177-50). Alignment of the detection optics was performed by positioning a thin quartz cell containing DCM (diluted in methanol) which absorbed in this wavelength region and produced a fourth wave visible to the unaided eye.

A fast (5Gs/s) digital oscilloscope LeCroy W44Xi and a PC were used to collect the data for further processing. The obtained spectra were calibrated using a wavemeter Burleigh WA-4500.

Figure 3.4. Schematic diagram of the experimental configuration used for performing DFWM measurements. The abbreviations used in here are defined as follows: M-mirror, L-lens, I-iris, P-prism, B-beamsplitter, PMT-photomultiplier tube.

As discussed above, both the linear CRD and nonlinear DFWM technique have their advantages and disadvantages. Moreover they complement each other. In this work, although not applied simultaneously, the units of the experiments were performed in such manner that one can easily switch from one to the other.

3.3 TWO-COLOR RESONANT FOUR-WAVE MIXING EXPERIMENT

Figure 3.5 shows a schematic diagram of the experimental setup. The output of dye laser (SCANmate 2E, Lambda Physik), pumped by the third harmonic of a Nd:YAG (Innolas Splitlight 600), was split into two pump beams with frequency ω_1 of equal intensity.
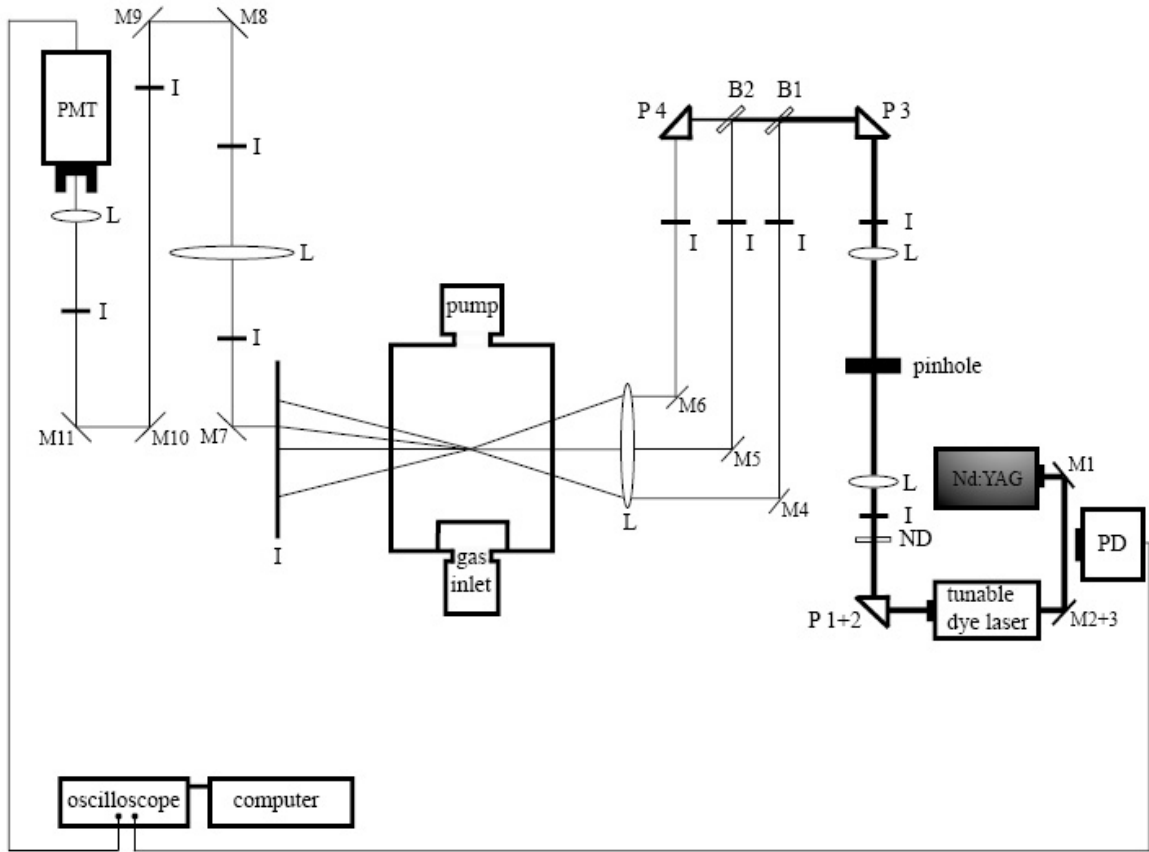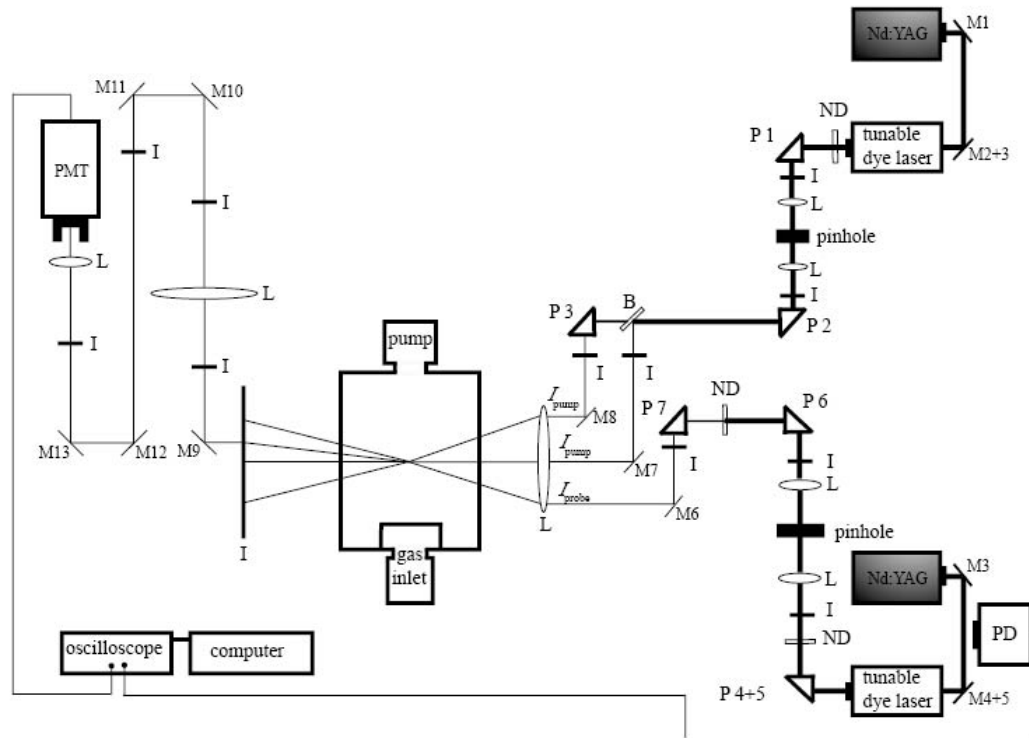

Figure 3.5. Schematic diagram of the experimental configuration used for performing TC-FWM measurements. The abbreviations used in here are defined as follows: M-mirror, L-lens, I-iris, P-prism, B-beamsplitter, PMT-photomultiplier tube.

These beams crossed the jet expansion ~ 5 mm downstream from the slit nozzle in a plane perpendicular to the jet axis and formed induced grating, shown in Figure 3.6. The true spatial interference pattern of the grating beams is more complex than the square plates shown in Figure 3.6. The grating fringes are parallel to the jet axis. The grating wave vector, $\mathbf{k}_g$, which is perpendicular to the fringes, is perpendicular to the axial jet velocity

($\mathbf{k}_g \mid \mathbf{v}_{jet}$). This orientation provides that the grating is long lived since it degrades only by the slow transverse motion in the jet. The configuration in which the grating fringes are perpendicular to the jet axis ($\mathbf{k}_g \parallel \mathbf{v}_{jet}$) forms grating that are rapidly washed out by the axial flow of the jet.
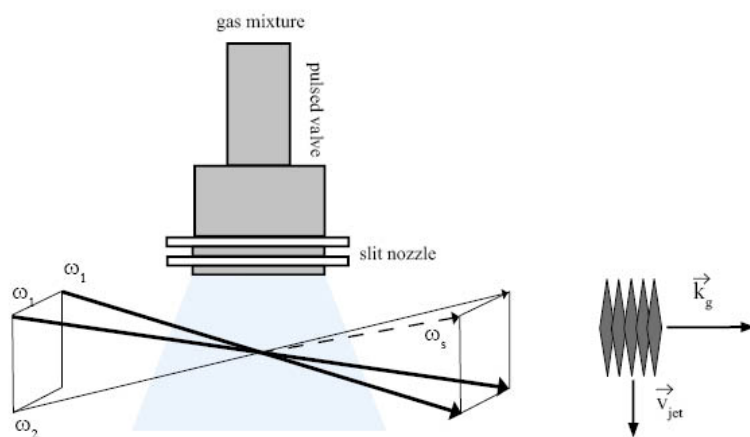

Figure 3.6. Scheme of the experimental arrangement used to obtain TC-LIGS spectra. The schematic picture of the population grating induced by the two beams at ω_1; the grating fringes are spaced ~15 μm apart and run parallel to the jet axis.

The probe laser radiation at ω_2 is produced by the second pulsed dye laser (JAGUAR, bandwidth ~ 0.1 cm^{-1}) tuned to an isolated rotational band. This laser output was spatially filtered and collimated a telescope before being directed to the interaction region. It crossed the induced grating at a small angle 2°. To avoid saturation effects the pulse energies were reduced to a few μJ for each of the input beams. The positions the pump and probe beams were adjusted to ensure spatial overlap at the focal region.

As in DFWM in the forward-box configuration, the diffracted signal beam was spatially separated from the grating beams and probe beam. The signal-beam collection optics and spatial filters were aligned by generating two-color LIGS signals at the interaction region in a thin cuvette containing a solution of dye (usually DCM) in methanol.

4 SPECTROSCOPY OF ALLYL RADICAL

4.1 STRUCTURE AND DYNAMICS OF THE ALLYL RADICAL

Figure 4.1 shows the allyl radical in a Cartesian coordinate system.
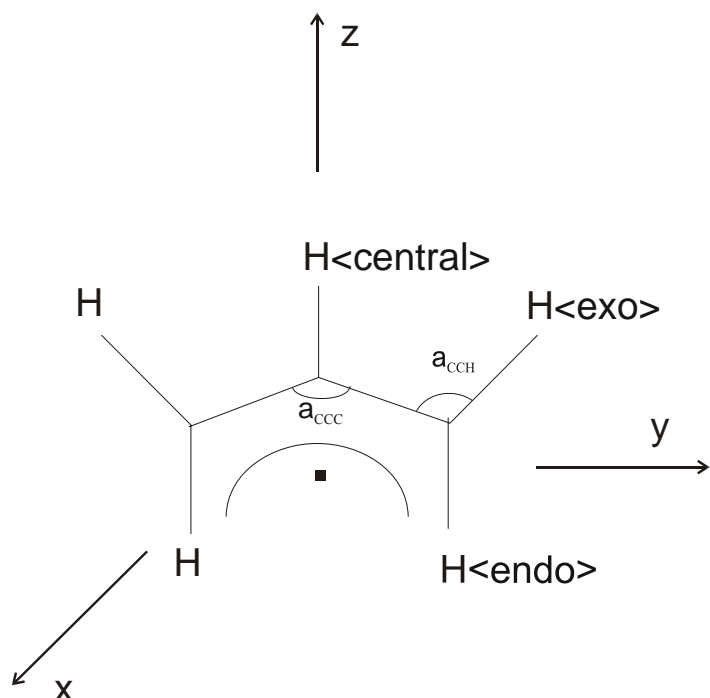
Figure 4.1 Valence bond picture of the allyl radical in a Cartesian coordinate system.

The allyl radical in its ground state belongs to the C_{2V} symmetry group, is planar in the yz-plane, has a C_2 axis along the z-coordinate and additional C_S symmetry in the xz and yz-planes. There are three distinguishable types of hydrogen atoms labeled $H_{central}$, H_{exo} and H_{endo}. The structure of the symmetric molecule is sufficiently described by the (C-C) bond length r_{CC}, the three (C-H) bond length $r_{CH}^{central}$, r_{CH}^{exo} and r_{CH}^{endo}, the (C-C-C) bond angle α_{CCC} and the three (C-C-H) bond angles $\alpha_{CCH}^{central}$, α_{CCH}^{exo} and α_{CCH}^{endo}.

The Hückel picture in Figure 4.2 illustrates the molecular orbitals and symmetries of the allyl radical ground and excited states. However, this description is rather qualitative

and no assumptions about the energies of the excited states should be drawn from this picture.
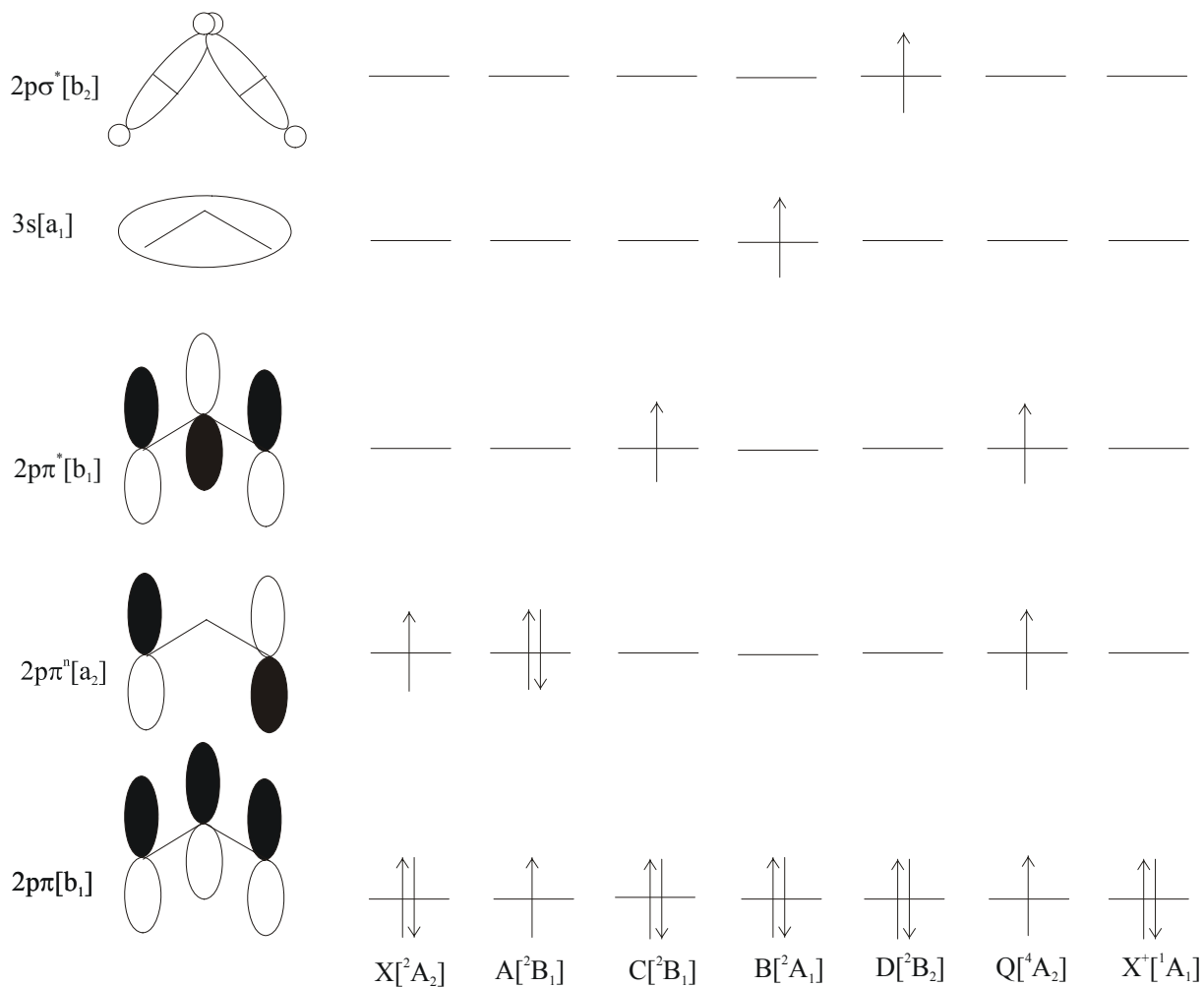
Figure 4.2 Hückel orbitals for allyl radical and the configurations of the excited states [66].

Experimental [67] and calculated [66] energies of the allyl radical excited states are given in the Figure 4.3. The calculations indicate that the lowest quartet state is well above all considered excited states, which excludes the possibility of an intersystem crossing in from the excited A, B, C or D state.
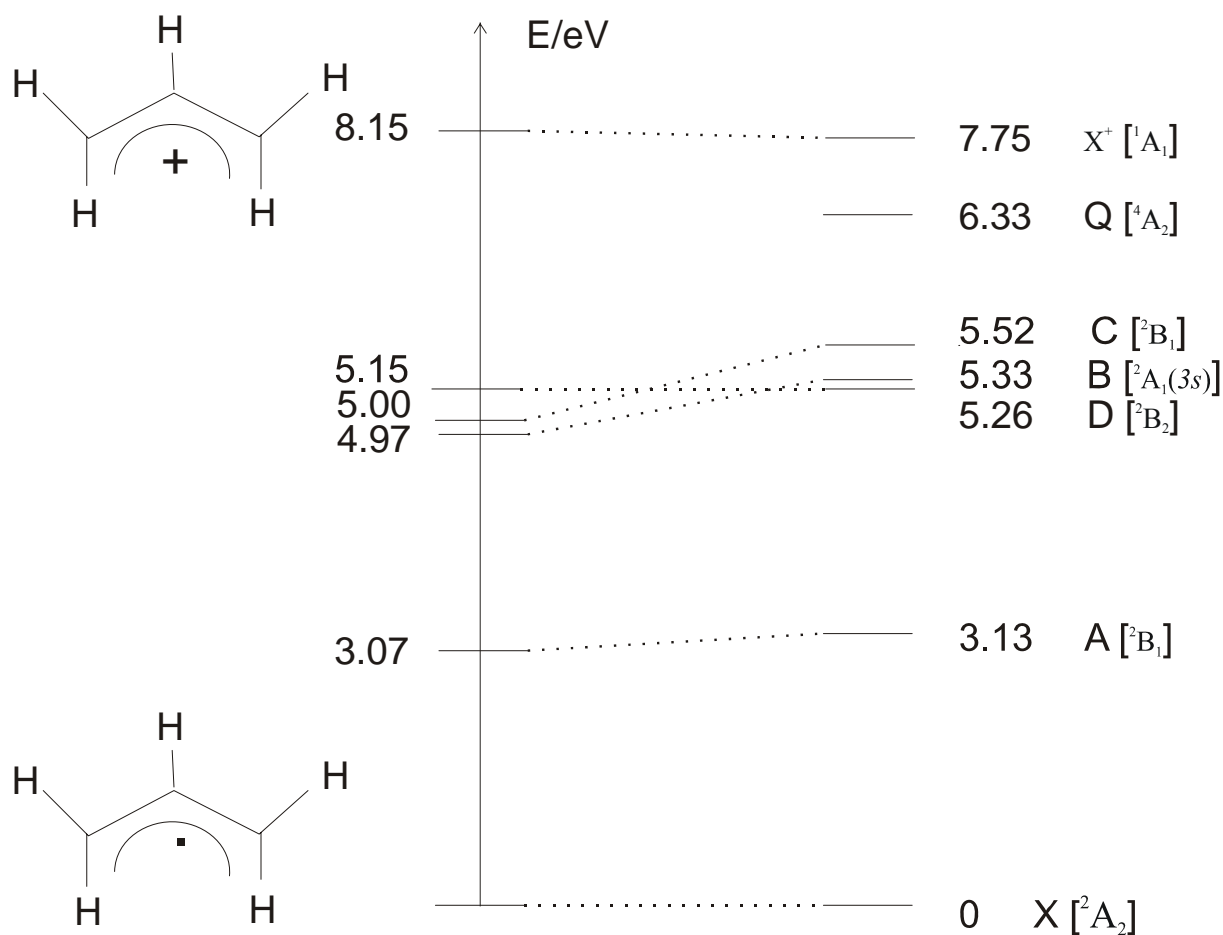
Figure 4.3 Electronic states of the allyl radical. Left: experimentally observed states, right: calculated ab initio energies and symmetry labels from [66].

4.2 GROUND AND EXCITED STATE PROPERTIES

The ground state structure of the allyl radical with C_{2v}-symmetry was derived from high-resolution infrared spectroscopy in the gas phase [68-70]. A (C-C) bond length of r_{CC}=1.3869±0.0033 Å and a (C-C-C) bond angle of α_{CCC}=123.96±0.48° was found, while the five parameters involving hydrogen atoms were assumed to take the ab initio values $r_{CH}^{central}$=1.087 Å, r_{CH}^{endo}=1.082 Å and r_{CH}^{exo}=1.085 Å. Vibrational frequencies have been measured by gas-phase resonance Raman experiments [71] and IR-spectroscopy in cryogenic matrices [72]. A list of the 18 vibrational modes and the corresponding frequencies in the ground state of allyl radical and the ground state of the allyl cation are shown in Table 4.1.

Table 4.1. Vibrational frequencies for the allyl radical ground state (X) [73]

	mode	assignment	frequency X (cm^{-1})
a_1			
	ν_1	asym. CH$_2$ stretch	3109
	ν_2	CH stretch	3028
	ν_3	sym. CH$_2$ stretch	3013
	ν_4	CH$_2$ scissors	1484
	ν_5	CH$_2$ rock	1245
	ν_6	CCC stretch	1017
	ν_7	CCC bend	416
a_2			
	ν_8	CH$_2$ out of plane bend	779
	ν_9	CH$_2$ twist (disrot.)	538
b_1			
	ν_{10}	CH out of plane bend	979
	ν_{11}	CH$_2$ out of plane bend	805
	ν_{12}	CH$_2$ twist (conrot.)	521
b_2			
	ν_{13}	CH$_2$ stretch	3105
	ν_{14}	CH stretch	3015
	ν_{15}	CH$_2$ scissors	1409
	ν_{16}	CH bend	1404
	ν_{17}	CCC stretch	1215
	ν_{18}	CCC rock	919

The lowest excited state (A state) with a tentatively assigned band origin at 24500 cm^{-1} was observed by flash photolysis absorption spectroscopy of numerous allyl radical precursors [74]. The lack of fluorescence and failed attempts to measure MPI spectra with nanosecond lasers indicated a short lifetime of this state. According to the

Woodward-Hoffmann rules, a cyclization reaction to cyclopropyl radical from the A state is allowed and evidence for this reaction was reported in irradiation experiments of allyl radical in noble gas matrices [75]. Recent *ab initio* calculations [76, 77] indicated the existence of two conical intersections between the A state and the ground state at (C-C-C) bond angles of 90-100º and with the methylene residues twisted in conrotatory or disrotatory fashion out of the molecular plane. Such structures may be on the reaction coordinate for the cyclization to cyclopropyl radical.

A complex band system to the blue of 250 nm was found in flash photolysis absorption spectroscopy [78]. Three overlapping electronic band systems could be observed in MPI spectra [79] and were later assigned by resonance Raman [80] and MPI spectroscopy [67, 81]. The lowest of the three states with a band origin at 40056.5 cm^{-1} was assigned as [$^2A_1$] *3s* Rydberg state (B state). The B[$^2A_1$] ← X[$^2A_2$] transition is formally one photon forbidden but was observed in the MPI spectra, indicating vibronic coupling to the two higher states and a geometric distortion of the B state. In a tentative simulation of the partially resolved rotational structure, a geometry with r_{CC}=1.40 Å, α_{CCC}=112.0º and a dihedral angle (twisting of the methylene groups put of the plane) of θ=20º was suggested [81].

The second state in the UV band system (C state), with a band origin at 40305.5 cm^{-1}, was assigned as a [$^2B_1$] state. In the Hückel approximation, this state is degenerate to the A state, but a large splitting of 2.5 eV was predicted in early configuration interaction calculations [82]. A fit of the rotational profile in the MPI spectra gave a planar geometry with r_{CC}=1.385±0.01 Å and α_{CCC}=116.5±1º [67, 81]. As in the case of the A state, cyclization to cyclopropyl radical is Woodward-Hofmann allowed and was repeatedly discussed in the literature [66]. Resonance Raman experiments at 224.63 nm, 4212 cm^{-1} above the C state origin were "in qualitative agreement with the theoretically predicted disrotatory photoisomerization of allyl radical" [71], but so far no unambiguous evidence for such a cyclization was reported in the literature.

The third state in the UV band system with a band origin at 41557.8 cm^{-1} was assigned as [$^2B_2$] state (D state). The D[$^2B_2$] ← X[$^2A_2$] transition is only weakly allowed, but strong vibronic coupling to the B and C states was observed in the resonance Raman experiments and is reflected in the observed intensities [80, 83].

No MPI spectrum could be observed to the blue of 240 nm, although the oscillator strengths in absorption spectra were found to increase with the excitation energy up to 224

nm [78]. It was suggested that a fast relaxation process might be in competition with ionization and quench the ion signal in the MPI spectra [67].

The lowest quartet state was calculated with a band origin at 51050 cm^{-1}, well above any of the excited states discussed so far. The adiabatic ionization potential for allyl radical was determined by HeI photoelectron spectroscopy to be 8.13 ± 0.002 eV [84].

4.3 RESULTS AND DISCUSSION

The gas-phase $A\ ^2B_1\leftarrow X\ ^2A_2$ electronic transition of the allyl radical was detected at 24492.1 cm^{-1} (Figure 4.4), which is consistent with the previous detection by the flash photolysis of allyl bromide that was carried out by Currie et al. [74]. Unfortunately, an analysis of the spectrum is difficult and was incorrectly presented in [85]. Later on a cw CRDS experiment with higher resolution was performed, which showed that apart from allyl there is another absorber in this range [86]. The rotationally resolved absorption spectrum was analyzed and assigned to a symmetric top molecule viz. $C_4H_3^+$. Thus, the previously observed spectrum of allyl was re-analyzed.
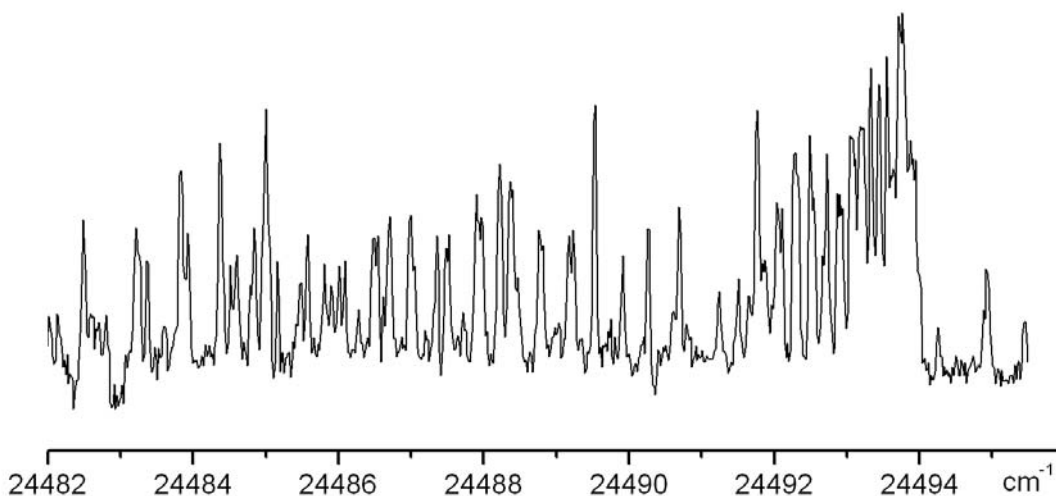
Figure 4.4. Rotationally resolved electronic absorption spectrum (0.06 cm⁻¹ resolution) of the origin band in the $\widetilde{A}\,^2B_1$- $\widetilde{X}\,^2A_1$ transition of C_3H_5 measured by CRD spectroscopy at 40 K.

The infrared diode laser kinetic spectroscopy experiment carried out by Hirota et al. shows that the allyl radical has C_{2V} symmetry in the ground state [69]. When it comes to the first excited state, two different geometries: C_2 (nonplanar), as a saddle point and C_{2V} (planar), as an equilibrium one were proposed. They were calculated by using the complete active space self-consistent field (CASSCF) method by Tonokura et al. [87] These *ab initio* calculations showed that both geometries were very close energetically.

The experimental conformation of the allyl structure was performed on the spectrum of C_3D_5 which could be more easily analyzed because in that region there were no significant disturbing overlapping lines from other species.

The electronic spectrum of the deuterated allyl species was measured for the first time (Figure 4.5.) in the gas phase. In this case C_2D_2 was used as a precursor gas. The $A^2B_1 \leftarrow X^2A_2$ electronic transition was detected at 24551.1 cm⁻¹, which is approximately 60 cm⁻¹ blue shifted with respect to the C_3H_5 band. However, because the rotational structure of the R-branch is not well resolved, a least-square fitting procedure called "total spectrum fitting" (TSF) was performed to obtain the molecular constants. The TSF method compares the observed and simulated rotational profiles. In this procedure a spectrum of an asymmetric top molecule is characterized only by the following parameters: rotational constants A, B, C of ground and excited states; transition frequency; temperature; spin

statistical weights; a FWHM of Gaussian line shape; an amplitude and base line bias (the slope was corrected before the analysis) [86].
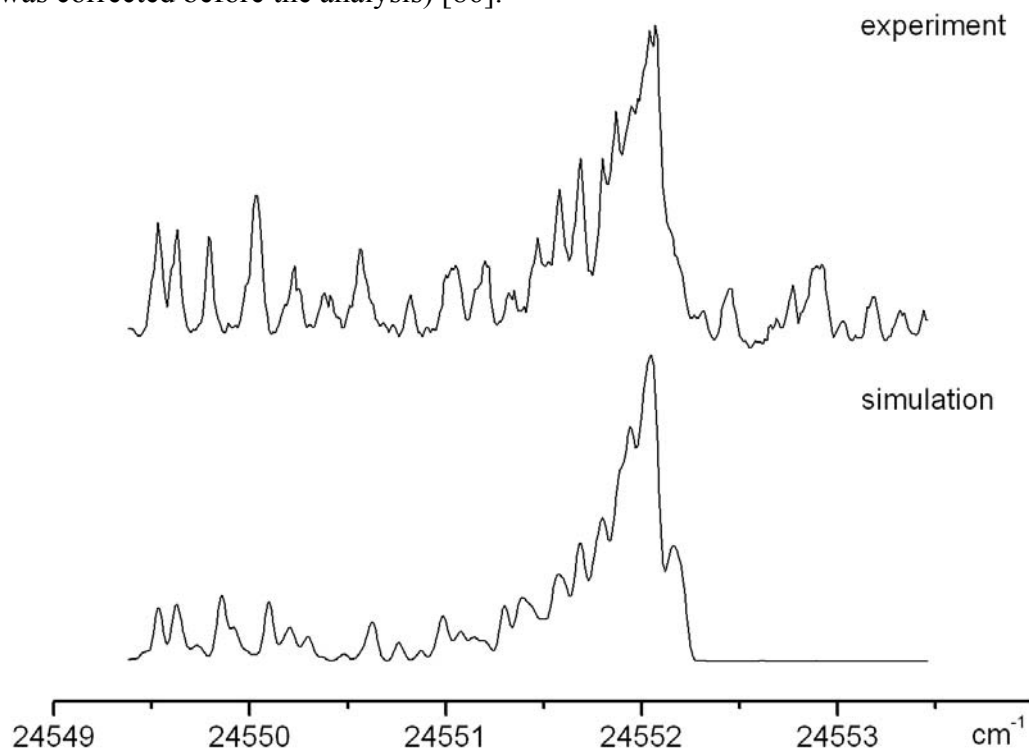
Figure 4.5. Electronic absorption spectrum, $\widetilde{A}\,^2B_1 \leftarrow \widetilde{X}\,^2A_2$, of the origin band of C_3D_5 (upper trace) measured by pulsed CRD spectroscopy and the simulated spectrum by the total spectrum fitting (TSF) method (lower trace).

To simulate the C_3D_5 spectrum lines through $J = 50$ have been used which is sufficient for the jet cooled spectrum. Absorption lines apparent in the recording (upper trace in Figure 4.5), except for the R-branch lines, were treated with zero-weight. The FWHM of Gaussian line shape was assumed to be 0.05 cm^{-1} due to Doppler broadening.

Rotational constants (A", B", C") for the ground state were fixed using the molecular structure of C_3H_5 determined by Hirota et al. [69] the spectrum of the ν_{11} vibrational band obtained in the 779 - 823.5 cm^{-1} region. The ratio of B and C in the excited state was also fixed. Best agreement with the experiment was attained with a rotational temperature of 25 K (lower trace on Figure 4.5). The rotational constants for the excited state determined from the analysis are listed in Table 4.2.

Table 4.2.Molecular constants of C_3D_5 obtained by the TSF method (cm^{-1}).

	this work	infrared [a]	*ab initio* [b]	
			C_{2v}	C_2
A''	1.1012 [c]	1.1012	1.1182	
$\frac{1}{2}(B''+C'')$	0.2473 [c]	0.2473	0.2475	
ΔA	-0.04187(4) [d]		-0.0558	-0.1504 [f]
$\Delta\frac{1}{2}(B+C)$	-0.029366(12) [d,e]		-0.0193	-0.0108 [f]
T_{00}	24550.3238(6) [d,g]			

[a] Values estimated from the molecular structure of C_3H_5 [69].
[b] CASSCF/TZV(d,p) in [87].
[c] Fixed.
[d] Values in parentheses denote the standard 2σ deviation.
[e] To calculate molecular structure of C_3D_5, separate values of B' and C' (0.241965 and 0.193843 cm^{-1}) were used.
[f] Differences between the ground C_{2v} and excited C_2 states.
[g] The error is from the least-squares fitting. Uncertainty of the calibration is 0.05 cm^{-1}.

The obtained rotational constants also proved that the allyl radical has a planar structure in the zero-point level of the excited state because the determined ΔA and $\Delta\frac{1}{2}(B+C)$ constants are closer to those predicted by *ab initio* calculations for C_{2V} rather than C_2 symmetry (Table 4.2). The obtained values were used to re-evaluate the C-C distance and CCC angle in the excited state of the allyl radical. Five structural parameters involving hydrogens were fixed to the *ab initio* values [87] in C_{2V} symmetry, $r(C_1D_1)$ = 1.072 Å, $r(C_2D_2)$ = 1.073 Å, $r(C_2D_3)$ = 1.071 Å, $\theta(D_2C_2C_1)$ = 120.4°, and $\theta(D_3C_2C_1)$ = 120.8°. This leads to $r(C_1C_2)$ = 1.4985±0.0064 Å and $\theta(C_2C_1C_3)$ = 124.51±0.31°. Errors are derived from an inertial defect.

Three vibrational bands of C_3H_5 were also observed in the region of 24588.7-4836.7 cm^{-1}. The observed bands were confirmed by recording the corresponding spectra of the isotopic species and two of them are shown in Figure 4.6 and 4.7.
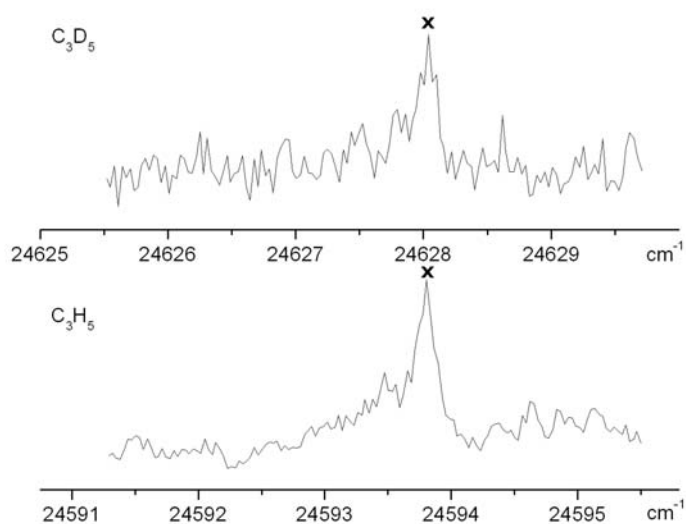
Figure 4.6. The 9_0^1 band in the $\widetilde{A}\,{}^2B_1$- $\widetilde{X}\,{}^2A_1$ transition of C_3H_5 and C_3D_5 measured by CRD spectroscopy (0.15 cm^{-1} resolution) using C_2H_2 or C_2D_2 as precursors in the discharge. Band heads of the **R**-branch are marked with **x**.
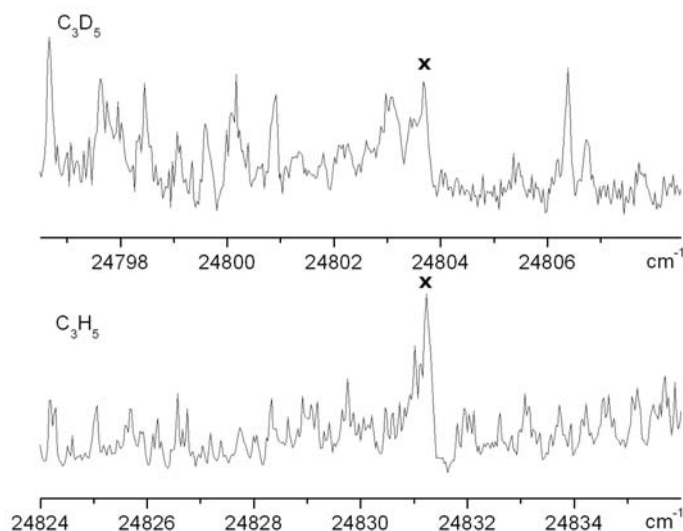
Figure 4.7. The 7_0^1 band in the $\widetilde{A}\,{}^2B_1$- $\widetilde{X}\,{}^2A_1$ transition of C_3H_5 and C_3D_5 measured by CRD spectroscopy (0.15 cm^{-1} resolution) using C_2H_2 or C_2D_2 as precursors in the discharge. Band heads of the **R**-branch are marked with **x**.

Because the electronic states have B_1 (for the excited state) and A_2 (for the ground state) symmetry, the transition moment must have b_2 symmetry. It is consistent that the observed origin band of C_3H_5 is of a-type transition (b_2 symmetry).

The resolution in the present experiment (0.15 cm^{-1}) allowed the type of each transition to be determined. All of them are assigned as an a-type transition, which indicates that the observed vibrational bands have an a_1 symmetry. The vibrational band positions and its frequencies are listed in Table 4.3.

Table 4.3. Vibrational band positions and its frequencies (cm^{-1}) of C_3H_5.

ν_{obs}	interval from (0-0) band
24599.6	108
24721.2	230
24831.8	341

51

5 SPECTROSCOPY OF PROPADIENYLIDENE

5.1 INTRODUCTION

Interest in investigation of hydrocarbon families like the cumulene carbenes ($H_2C(=C)_n$) arises from their relevance in combustion [88] and photochemical [89, 90] processes as well as their detection in the interstellar medium. Several members with n = 2-8 have been detected in the laboratory by microwave spectroscopy and n = 2, 3, 5 in dark molecular clouds [91]. In the literature cumulene carbenes have also been suggested as possible diffuse interstellar bands (DIBs) carriers [92]. Consequently the electronic spectra of these species in the gas phase are required. The first electronic spectrum of propadienylidene $H_2C=C=C$: was recorded in an argon matrix [89] and later on the vibrationally resolved spectrum was observed in solid neon [93]. Three electronic transitions were observed: a strong $\widetilde{C} - \widetilde{X}$ band system in the 39051-47156 cm^{-1} range, weaker $\widetilde{B} - \widetilde{X}$ transition in the 16161-24802 cm^{-1} region, and the hardly detectable forbidden $\widetilde{A} - \widetilde{X}$ one at 13885-16389 cm^{-1}. Based on these observations one can search for these absorptions in the gas phase.

In this work the electronic spectrum of propadienylidene has been measured using cavity ring down spectroscopy (CRDS). The stronger $\tilde{B}\ ^1B_1 - \tilde{X}\ ^1A_1$ transition has not been observed presumably because the short lifetime of the $\widetilde{B}$ state leads to broad absorptions which are difficult to detect. Two forbidden vibrational bands in the $\tilde{A}\ ^1A_2$ - $\tilde{X}\ ^1A_1$ system are however seen. The transition at 15813 cm^{-1} gains intensity through a-type Coriolis coupling in the excited state, and the one at 16233 cm^{-1} borrows intensity by vibronic coupling with the nearby states of appropriate symmetry. The rotational analysis carried out gives the molecular constants for the excited state, which can be used to calculate a geometrical structure.

5.2 FORBIDDEN TRANSITIONS

5.2.1 Transitions due to vibronic interaction

In forbidden electronic transitions which occur on account of vibronic interactions certain vibrational transitions may occur weakly if they are in accordance with the vibronic selection rules. The principal cause of the intensity in forbidden electronic transitions is mixing of electronic states by vibrations. The general theory of these interactions was developed by Herzberg and Teller [94, 95]. At that time, however, too little was known about electronic wave functions for quantitative applications to be possible. More recently J. A. Pople and J. W. Sidman published a theoretical survey of vibrationally induced intensity in the formaldehyde transition [96]. The transition moment and thus the band structure is determined by the vibronic symmetry of upper and lower state. For example, the $^1B_2 - {^1A_1}$ vibronic transition of C_3H_2 in the $^1A_2 - {^1A_1}$ forbidden electronic transition of point group C_{2V} has the structure of the $^1B_2 - {^1A_1}$ electronic band.

5.2.2 Transitions induced by Coriolis interaction

It is well known that the separation of electronic motion and molecular rotation is not rigorous. The failure of this Born-Oppenheimer separation can lead to an observable breakdown of the selection rules.

Consider the $^1A_2 - {^1A_1}$ electronic transition of C_3H_2 which has a C_{2V} symmetry. Such transition is rigorously forbidden in the non-rotating molecule. However, if the A_2 state is near a third state that can combine with A_1, the state A_2 may mix with this third state with increasing rotation and will therefore allow its higher rotational levels to combine with A_1. In the case of C_3H_2 this third state is a B_1 state and it is rotation about the x-axis can cause mixing. If the *z*-axis is the *a*-axis levels differing by ± 1 in K_a, the levels can then perturb one another. Figure 5.1 shows an energy level diagram for this case.
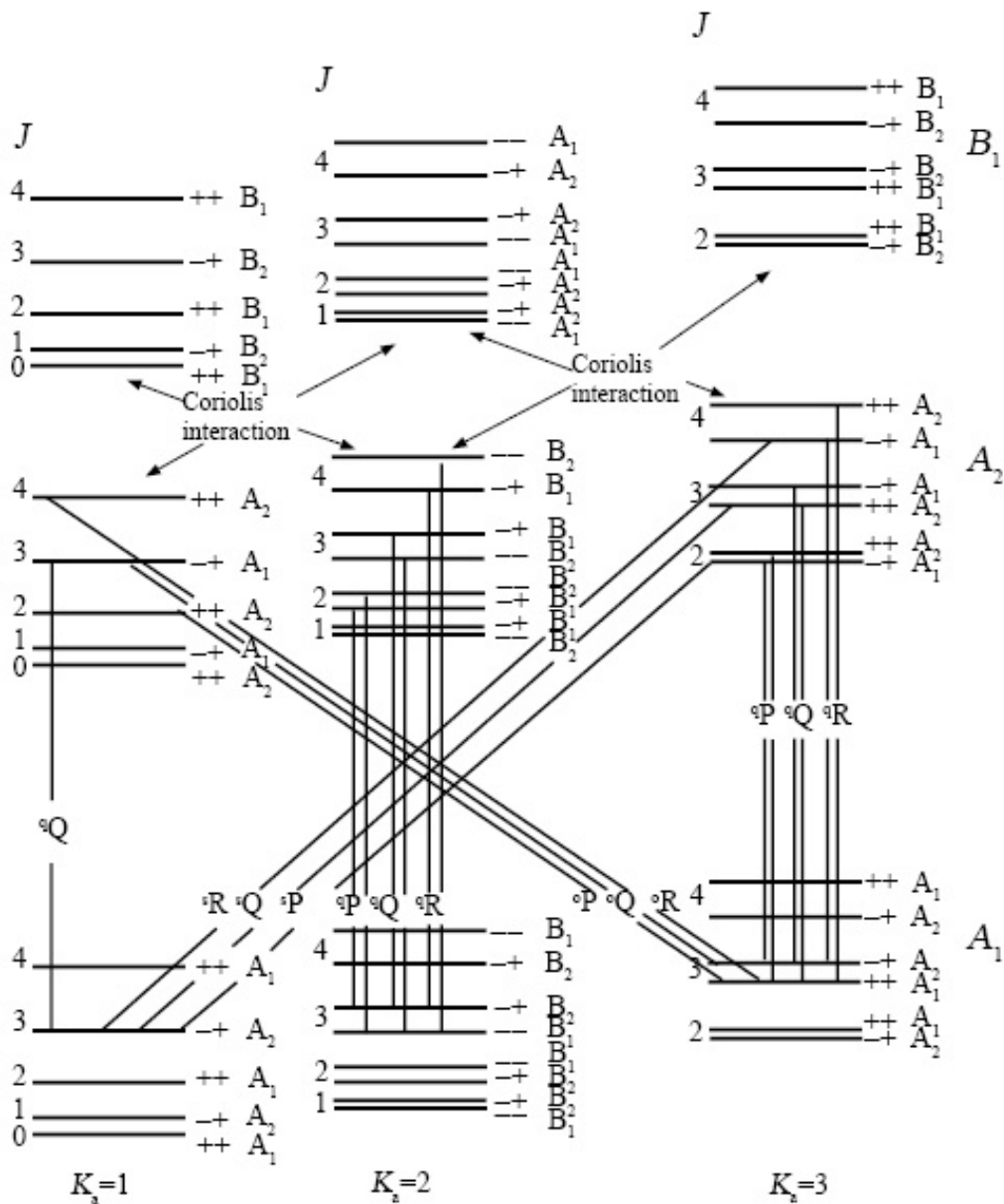
Figure 5.1. Rotational transitions due to Coriolis interaction in a forbidden ($A_2 - A_1$) electronic transition of a C_{2v} molecule (e.g. C_3H_2). The interacting state is shown at the top. The arrows indicate which rotational levels can interact with each other. Only one line of each branch is shown in the lower part [95].

Coriolis perturbations can take place only between states of the same J and the same rovibronic species [95]. Therefore, as Figure 5.1 shows, the A_2 vibronic levels with $K_a = 0$, 1,

2, mix with the B_1 levels with $K_a = 1$, 0 and 2, 1 and 3, etc. and therefore transitions with $\Delta K_a = 0$, ± 2 arise. In the theoretical investigation of the Coriolis effect [96] it was shown that the intensity of the forbidden electronic transition induced by rotation is proportional to K_a^2. Thus, the $K_a = 0 \leftarrow 1$ subband will be absent in the spectrum.

5.3 RESULTS AND DISCUSSION

In this work two rotationally resolved vibronic bands in the forbidden $\tilde{A}\,^1A_2 - \tilde{X}\,^1A_1$ electronic transition of the cumulene carbene C_3H_2 have been observed by means of CRDS.
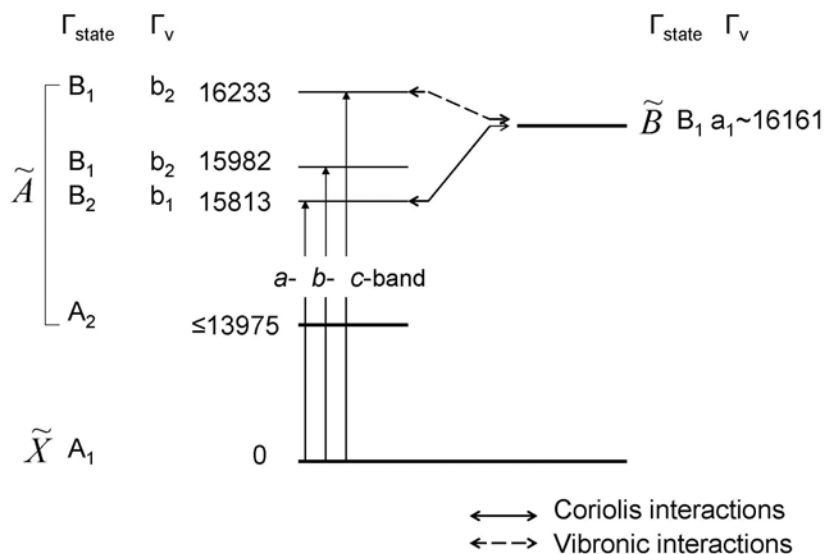

Figure 5.2. Energy level diagram (cm^{-1}) showing the possible vibronic and Coriolis interactions.

The first transition (in following called c-band, see Figure 5.2) was detected around 16233 cm^{-1}. It consists of three subbands $K_a = 0 \leftarrow 1$, $K_a = 1 \leftarrow 0$, and $K_a = 2 \leftarrow 1$ as shown in Figure 5.3.
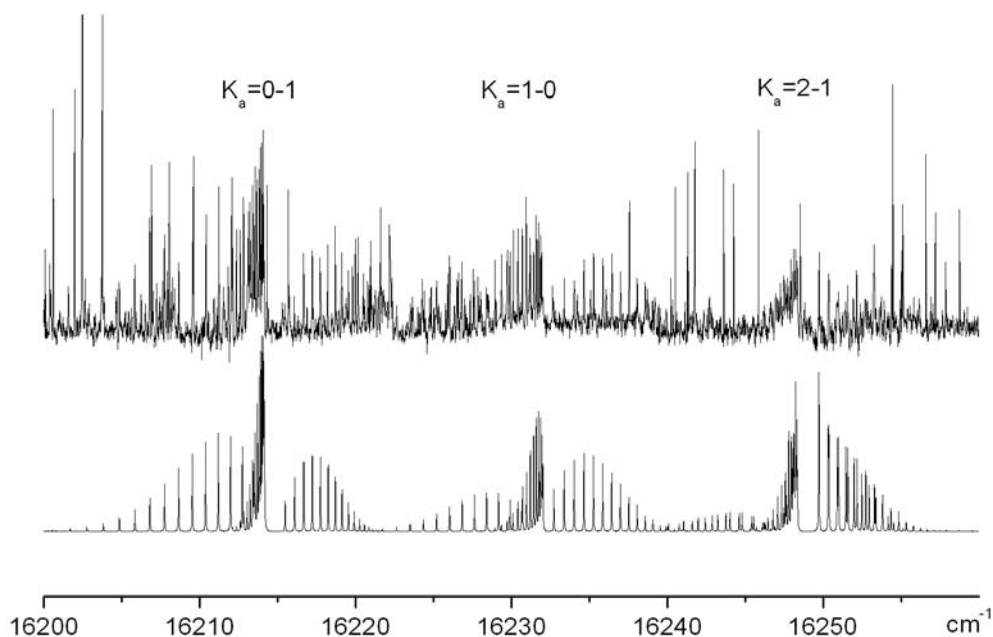
Figure 5.3. Rotationally resolved electronic absorption spectrum of the *c*-band in the $\widetilde{A}$ $^1A_2$ - $\widetilde{X}$ $^1A_1$ transition of H_2CCC (upper trace) and the simulation (lower trace) at 20 K.

Initially the *P*-, *Q*-, and *R*-branches of the three subbands were fitted to a polynomial. A least-squares fit to the frequencies of 76 lines was made with a conventional rotational Hamiltonian for an asymmetric top molecule without centrifugal distortion terms using the program WANG. The obtained rotational constant $\frac{1}{2}(B''+C'')$ for the ground state matched with the microwave value within error in the initial fitting (Fit I in Table 5.1). The agreement of rotational constants confirmed that the observed transition is due to the H_2CCC species. It was assigned to the forbidden electronic transition $\widetilde{A}$ $^1A_2$ - $\widetilde{X}$ $^1A_1$ because of its weak intensity. In the next step the ground state B'' and C'' constants were fixed to the microwave values [97]. The A'' constant was taken from [98], where it was determined from the separations of the subbands using high resolution cw-CRD spectroscopy. The result of this is Fit II in Table 5.1

Table 5.1. Molecular constants (cm^{-1})^{a} of H$_2$CCC.

State	Constant	a-band		b-band[b]	c-band		microwave[c]
		Fit I	Fit II	Fit II	Fit I	Fit II	
$\widetilde{X}\,^{1}A_1$	A"	9.6451^{d}	9.6451^{d}	9.6451(17)	9.6688(28)	9.6451^{d}	9.6328(11)
	B"	0.35326(22)^{e}	0.353198^{f}	0.353198^{f}	0.35315(14)^{e}	0.353198^{f}	0.353198(67)
	C"	0.34043(22)^{e}	0.340367^{f}	0.340367^{f}	0.34075(14)^{e}	0.340367^{f}	0.340367(67)
	½(B"+ C")	0.34681(22)			0.34695(14)		0.346783(67)
$\widetilde{A}\,^{1}A_2$	A'	8.7525(39)^{g}	8.7526(37)^{g}	9.83717(46)	8.8987(10)	8.8977(16)	
	B'	0.34076(46)	0.34070(22)	0.341217(86)	0.34204(15)	0.341750(91)	
	C'	0.33046(46)	0.33039(15)	0.328764(91)	0.32883(14)	0.328695(49)	
	T$_{00}$^{h}	15812.792(10)	15812.7913(95)	15982.0367(16)	16223.4777(32)	16223.4673(40)	

^{a} Values in parentheses denote the standard deviation.
^{b} Ref [98].
^{c} Ref [97].
^{d} Fixed to the value of [98].
^{e} Ratio between B and C constants is fixed to that of [97].
^{f} Fixed to the value of [97].
^{g} accurate determination of this value is hindered by the Coriolis interaction.
^{h} Error arises from the least-squares fitting and 0.05 cm^{-1} uncertainty of the calibration.

The simulated spectrum with the constants from Fit II and a single Boltzmann population for the two nuclear spin isomers is shown in Figure 5.3. The intensity distribution of the *K*-structure is in agreement with the observation. An independent Boltzmann population model fails because (i) the laser beam crossed the supersonic jet 2 mm downstream from the slit nozzle, where the collisions between H$_2$CCC and the rare gas are still occurring. Thus, full collisional equilibration has not been attained. (ii) The observed transition is vibronically induced (see following), and thus the intensities are affected by vibronic interaction with the nearby $^{1}B_1$ state.

As the detected band is a c-type transition, the vibrational component in the upper state belongs to b$_2$ symmetry and the vibronic symmetry is B$_1$. Thus, the intensity is borrowed from the strong $\widetilde{B}\,^{1}B_1$ - $\widetilde{X}\,^{1}A_1$ transition by vibronic coupling. It might also interact with the nearby vibrational level in the $^{1}A_2$ state, which also has B$_1$ symmetry [98] as shown in Figure 5.2.

In a previous work *ab initio* calculations of the vibrational frequencies for the $^1A_2$ state were carried out using the CASSCF method [98]. From these results the investigated band can not be uniquely identified. The lowest energy peak in the $\widetilde{A}$ $^1A_2$ - $\widetilde{X}$ $^1A_1$ transition in the neon matrix spectrum is at 13975 cm^{-1} [93]. Thus the vibrational frequency of the *c*-band should be ≥2000 cm^{-1}, even taking into account a matrix-gas shift of around 100 cm^{-1}. According to symmetry and frequency the following combinations of vibrational modes are possible: (i) $\widetilde{v}_4$ (a$_1$) + $\widetilde{v}_8$ (b$_2$): 1983 cm^{-1}, (ii) $\widetilde{v}_3$ (a$_1$) + $\widetilde{v}_8$ (b$_2$): 2377 cm^{-1}, (iii) $\widetilde{v}_2$ (a$_1$) + $\widetilde{v}_8$ (b$_2$): 2648 cm^{-1}.

The second transition (*a*-band) was observed at 15813 cm^{-1}. It has an unusual rotational structure: the K_a = 0←1 subband is missing (Figure 5.4). The high-resolution spectrum has been analysed in a similar manner as described for the *c*-band. Based on Fit I the observed transition is assigned to the $\widetilde{A}$ $^1A_2$ - $\widetilde{X}$ $^1A_1$ vibronic transition of H$_2$CCC. Fit II (ground state constants fixed to the values from [97]) provided excited state rotational constants which are listed in Table 5.1.
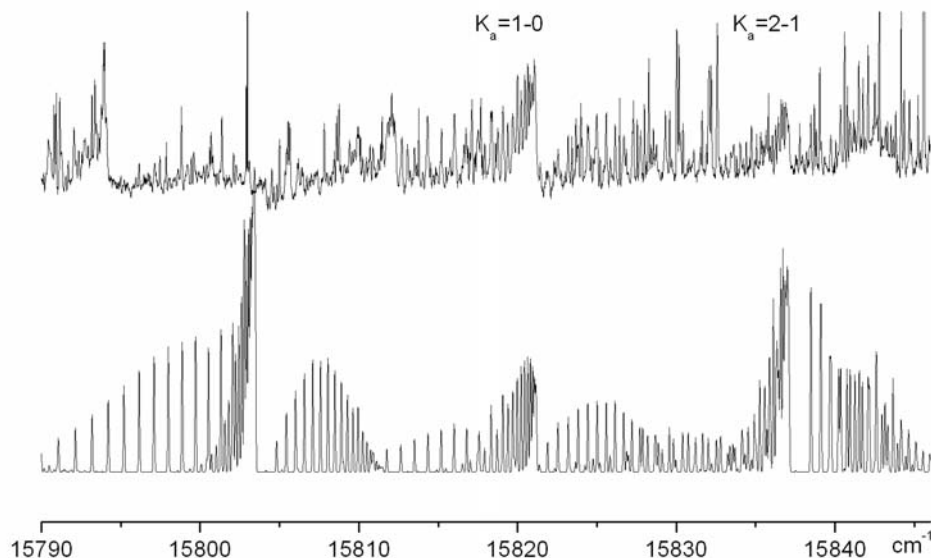
Figure 5.4. Rotationally resolved electronic absorption spectrum of the *a*-band in the $\widetilde{A}\ ^1A_2$ - $\widetilde{X}\ ^1A_1$ transition of H_2CCC (upper trace) and the simulation (lower trace) at 20 K. The K_a=0-1 structure is missing due to a-type Coriolis perturbation.

As already discussed above the missing $K_a = 0 \leftarrow 1$ subband suggests that intensity is borrowed through an *a*-type Coriolis interaction. This absence cannot be explained by an abnormal Boltzmann population of the *K* - levels because a $K_a = 0 \leftarrow 1$ subband appears clearly in the simulated spectrum.

Because the observed band is a c-type transition and considering *a*-type Coriolis interaction, the symmetry of the present vibronic state is B_2 with a b_1 vibrational component. Thus the observed transition borrowed its intensity through an interaction with nearby states with B_1 vibronic symmetry (Figure 5.2). The vibrational frequency should be $\geq 1600\ \text{cm}^{-1}$ even though a gas-matrix shift exists. A trial vibrational assignment gives rise to the following possible combinations: (i) $\widetilde{v}_3\ (a_1) + \widetilde{v}_5\ (b_1)$: 1966 cm^{-1}, (ii) $\widetilde{v}_2\ (a_1) + \widetilde{v}_6\ (b_1)$: 2044 cm^{-1}, (iii) $\widetilde{v}_2\ (a_1) + \widetilde{v}_5\ (b_1)$: 2237 cm^{-1} [98].

The obtained rotational constants were used to determine the molecular structure of the C_3H_2. According to the analysis of the millimetre-wave spectrum [99] H_2CCC in the ground state is a near prolate top with C_{2V} symmetry. The inertial defect Δ calculated from the rotational constants is just 0.0515 amu Å^2 implying a near planar species.

To follow the structural changes upon electronic excitation, Δ was calculated for the *a* and *c* observed transitions. As shown in Table 5.2, the structure is no longer planar when the *a* transition is excited, suggesting that one of the out-of-plane vibrations of b_1 symmetry is

involved, as already indicated from the rotational analysis. The inertial defect for the *c* transition was calculated to be 0.0645 amu $Å^2$ implying that the molecule remains planar in the upper electronic state.

Table 5.2. Molecular structure and inertial defect of H_2CCC. [a]

state	band	Δ [b]	bond length (Å)				angle (°)
			C_1-C_2	C_2-C_3	C_1-C_3	C_3-H	C_2-C_3-H
$\widetilde{X}$ $^1A_1$	0 [c]	0.0515	1.291	1.324	2.615	1.098	118.8
$\widetilde{A}$ $^1A_2$	*a*-band	-0.3827	1.3109(58)	1.367 [d]	2.6779(58)	1.082 [d]	115.387(12) [e]
	b-band		1.2948(24)	1.367 [d]	2.6618(24)	1.082 [d]	121.5511(35)
	c-band	0.0645	1.3092(11)	1.367 [d]	2.6762(11)	1.082 [d]	116.3584(20)

[a] Values in parentheses denote the standard deviation.
[c] Ref [97].
[d] fixed to the *ab initio* values for the $^1A_2$ state in [98].
[e] accurate determination of this value is hindered by the Coriolis interaction.

The rotational constants were used to determine the structural parameters for the $^1A_2$ excited state of propadienylidene species. The $r(C_2$-$C_3)$ and $r(C_3$-H) distances were fixed to the *ab initio* values. The bond length r $(C_1$-$C_2)$ and angle θ $(C_2$-C_3-H) were new determined to be 1.31 Å, 115.39° and 1.31 Å, 116.36° for the *a* and *c* transitions respectively (Table 5.2).

6 DEGENERATE FOUR-WAVE MIXING WITH THE SLIT EXPANSION

6.1 SPECTROSCOPY OF C_2

The spectroscopic properties of the (0, 0) $d\,^3\Pi_g \rightarrow a\,^3\Pi_u$ electronic transition of the C_2 are very well known. This so called Swan band system of C_2 has been investigated numerous times since the work of Wollaston (1802) and Swan (1857) almost two centuries ago. The literature on the Swan system is enormous. There was controversy about the emitter of the band system until King and Birge analyzed the Swan bands of the $^{12}C^{13}C$ molecule [100]. The vibrational analysis of the main bands of the system was given by Mecke [101], Johnson [102] and Shea [103]. Herzberg [104] correctly identified the high pressure bands of C_2 to be the v' = 6 progression of the Swan system, and Phillips [105] observed and identified several "tail" bands of this system. Many early investigators including Shea [103] and Mulliken [106, 107] attempted the rotational analysis of these bands. Although Johnson and Asundi [108] measured the rotational structure of some of the high-pressure bands, a complete rotational analysis was not published. Phillips [105] performed the rotational analysis of the tail bands of this system and later Burgrim et al. (1965) observed four more bands. Phillips and Davis published a complete atlas of the Swan system.

To date, measurements done with the FWM technique have been carried out only on high temperature (3000 K) oxy-acetylene flames [109-111]. The experiments on C_2 described here aimed to test the built DFWM and TC-RFWM apparatus coupled with a slit nozzle jet expansion and investigate the saturation effects in such type of experiments.

6.2 RESULTS AND DISCUSSION

Figure 6.1 shows a high resolution DFWM spectrum covering almost the entire (0, 0) $d\,^3\Pi_g \rightarrow a\,^3\Pi_u$ Swan band of C_2.
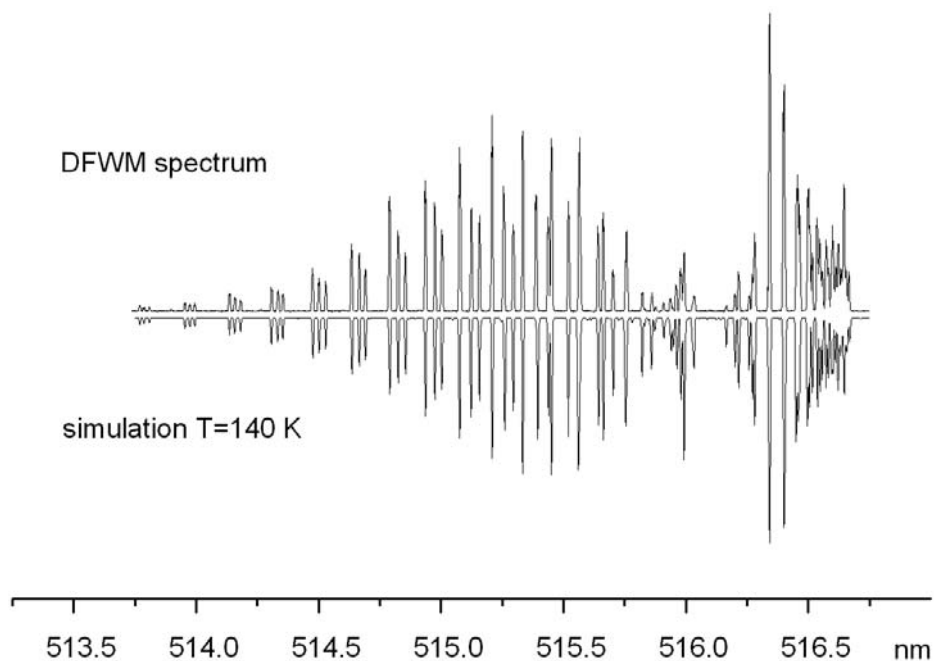
DFWM spectrum

simulation T=140 K

513.5   514.0   514.5   515.0   515.5   516.0   516.5   nm

Figure 6.1. DFWM spectrum of the (0, 0) $d\,^3\Pi_g \rightarrow a\,^3\Pi_u$ Swan band of C_2 and the simulation at 140 K.

Owing to small rotational constant (B ~ 1.6 cm^{-1}) the spectrum has a high density of lines and the data demonstrated the spectral resolution afforded by DFWM apart from the laser. Other vibronic transitions were readily detected within the dye range. The simulation gives an estimate of the Doppler temperature of about 140 K. The excellent signal-to-noise ratio on the order of 10^4 near the strongest transitions, is achieved by suppressing noise from scattered light by allowing the signal beam to propagate roughly 4 m through several irises and optical and

spatial filters. For these reasons the technique provides an excellent tool to test the accuracy of published line positions obtained both from theory and previous experimental data which is mostly limited by Doppler broadening.

Figure 6.2 shows the (0, 0) $d\,^3\Pi_g \rightarrow a\,^3\Pi_u$ Swan band of C_2 spectrum recorded by DFWM at a lower plasma temperature (approximately 50 K); to achieve this the discharge voltage was lowered to -400 V and the probed region was approximately 12 mm downstream from the nozzle slit. This resulted in a lower signal-to-noise ratio because of lower signal intensity due to lower species concentration. This exemplifies the potential of DFWM for probing plasma conditions in luminous and hostile environments.
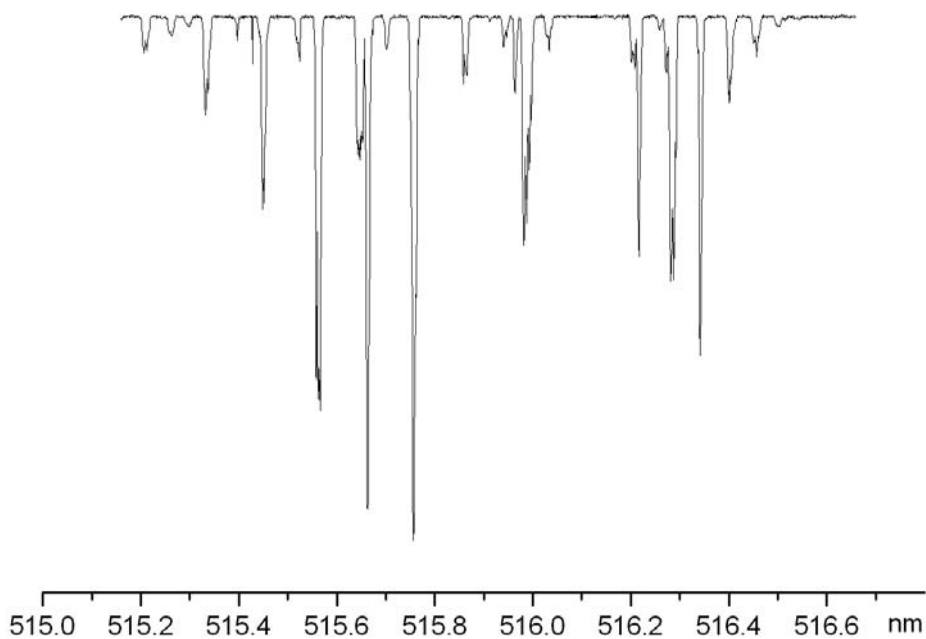

Figure 6.2. DFWM spectrum of the (0, 0) $d\,^3\Pi_g \rightarrow a\,^3\Pi_u$ Swan band of C_2 at 50 K.

6.2.1 Saturation effects

As was discussed above the highest signal to noise ratio in DFWM are obtained when the $I \approx I_{sat}$. In order to quantify saturation, intensity power measurements have been performed on two isolated transitions of C_2 at 515.076 nm $R_1(8)$ and at 515.121 nm $R_2(7)$ (Figure 6.3). The laser energy was varied manually by using neutral density filters.
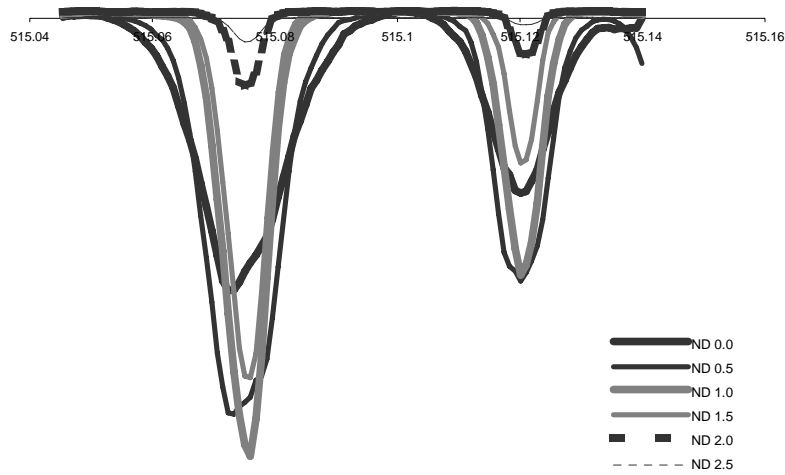
Figure 6.3. Saturation intensity power measurements on the two isolated transitions of C_2 $R_1(8)$ at 515.076 nm and $R_2(7)$ at 515.121 nm. ND-neutral density filters have been used to vary the power of incident radiation.

Figure 6.4 shows a variation of DFWM intensity at line center with laser power. A least linear fit on the first points leads to a slope of about 1.3. By fitting with equation (1.22), we could estimate an experimental value for I_{sat} at line center equal to 19 μJ per laser pulse, approximately.
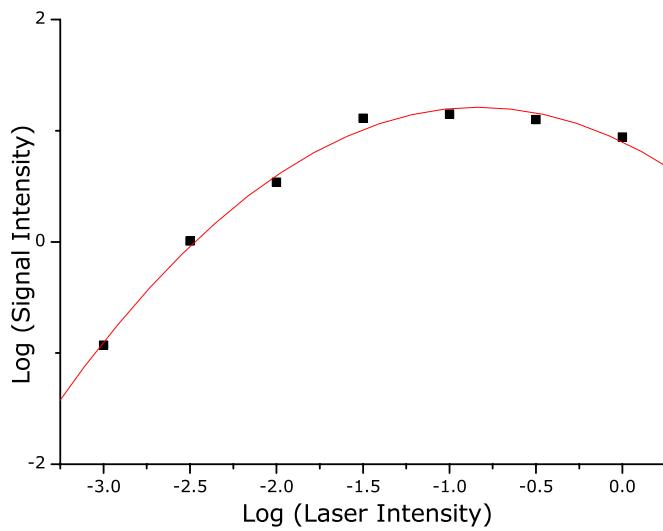
Figure 6.4 Saturation behavior of DFWM signal. A line fit through the first 4 points yields a slope of about 1.3. For higher laser intensities partial saturation behavior is evident.

Because only low intensities are required, the Keplerian telescope could be used which reduced the overall intensity substantially but yielded a very uniform circular near Gaussian intensity profile. This gives the advantage in shot to shot stability of the DFWM signals.

6.2.2 Comparison between CRDS and DFWM on C_2

In the following both CRDS and DFWM spectra of the $d\,^3\Pi_g \to a\,^3\Pi_u$ Swan band of C_2 are presented. The advantages and disadvantages of the techniques are discussed.

For comparison of sensitivity in the linear and non-linear techniques, DFWM and CRDS spectra of the Swan transition are presented in Figure 6.6. It is known that the expansion conditions in the molecular beam apparatus differ for different experiments. Even though the backing pressure and C_2H_2/Ar mixture are carefully controlled, a specific final rotational temperature is difficult to achieve. Therefore, we have not been able to perform both experiments at exactly the same temperature. Due to the geometrical parameters in the forward box configuration in the DFWM experiment, the laser radiation probes the gas flow 2 mm lower compared with the distance in CRDS. Moreover, in the DFWM case the lines are slightly saturated which is hard to avoid. Nevertheless, a direct comparison is interesting and yields additional information.
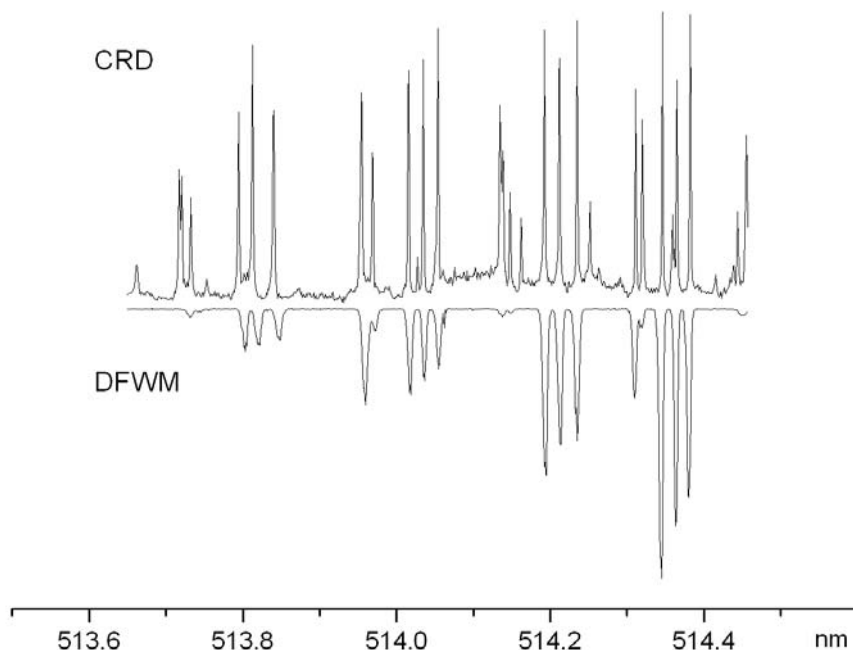

Figure 6.6. Comparison of CRDS (upper trace) and DFWM (lower trace) a part of the spectrum of the Swan transition of C_2. In the case of DFWM the square root of the FWM signal is shown.

66

The DFWM seems to have more sensitivity because the fluctuations of the baseline are smaller. The CRD spectrum of C_2 are obtained with signal-to-noise ratio (SNR) about 130:1 for the strongest transitions (Figure 6.6), where SNR in the DFWM experiment is about 1100:1. Moreover the DFWM spectrum is more structured with ordered line intensities. Due to the fact that the signal in the CRDS experiment is generated over the whole length of the slit by traversing the laser beam a large number of times through the plasma, i.e. probing molecules under different conditions, there are some additional lines are seen on the spectrum with randomly intensities. The interaction volume in the DFWM experiment is defined by the overlap between three incident radiations which is in this work ~ 2 cm.

Thus, an advantage of DFWM is that one records background free spectra in a properly aligned experimental setup, and, in case of phase-conjugated configuration, also Doppler-free. Because the spectra obtained by DFWM are very well structured it simplifies their assignment and analysis.

The CRDS setup used in this work does not allow the selective study of molecules. Instead, all species produced in the plasma are observed simultaneously, and thus one must determine if the observed spectral features belongs to the molecule of interest. Overlapping transitions can make assigning the spectrum nearly impossible. Thus, not having enough laser resolution resulted in misassigning the spectrum of allyl radical [85]. In the DFWM experiment the signal is much more sensitive to the experimental parameters, such as the distance between the laser beam and the slit nozzle, the applied voltages, the delay between the valve and discharge, etc. Moreover, because the signal intensity is proportional to the second order of the total number of absorbing species, one can expect that different absorbers can be more easily distinguished.

The major advantage of cavity ring-down spectroscopy compared to DFWM is the experimental setup. A CRDS experiment is easily performed since no special optical components are required. The alignment is straightforward and no major difficulties are encountered.

7 DFWM AND TC-RFWM ON HC$_4$S

7.1 INTRODUCTION

Interest in studying sulfur-bearing conjugated hydrocarbons arises not only due to their astrophysical relevance, but also their applications in molecular electronic devices.

Sulfur terminated the carbon chains add strong polarization to the π-system, resulting in a strong dipole moment and consequently a large electronic oscillation strengths. Because of the sufficient abundance of sulfur in the interstellar medium one can expect the sulfur containing species to be found there. Sulfur-bearing molecules such as C$_3$S and C$_5$S have been already detected in the space by radioastronomy [112-114].

Up to now the optical spectra of the first five members of the HC$_{2n}$S family have been measured. Thus, HC$_2$S, HC$_4$S, HC$_6$S have been studied by means of LIF [115-117], where the spectrum of the HC$_6$S has been also recorded by two-color two-photon ionization [118]. HC$_8$S and HC$_{10}$S were studied by CRDS [118].

Recently, the spectrum of the $\tilde{A}\,^2\Pi_{3/2} \leftarrow \tilde{X}\,^2\Pi_{3/2}$ system of HC$_4$S, produced in a supersonic discharge, has been studied by LIF [116] and dispersed fluorescence [119]. In the latter, the authors report an extensive study of several vibronic transitions, while in the former a rotationally resolved spectrum was observed with a 0.02 cm^{-1} laser linewidth, allowing spectroscopic constants to be determined. However in their experiment the $\tilde{A}\,^2\Pi_{1/2} \leftarrow \tilde{X}\,^2\Pi_{1/2}$ spin-orbit component was not observed due to low temperatures in the jet.

7.2 RESULTS AND DISCUSSION

HC$_4$S and DC$_4$S have been synthesized by discharging a mixture of 0.3% C$_2$H$_2$ (or C$_2$D$_2$), 0.1 % CS$_2$ in carrier gas Ar. Figure 7.1 shows the measured $\widetilde{A}\ ^2\Pi_{3/2} \leftarrow \widetilde{X}\ ^2\Pi_{3/2}$ and $\widetilde{A}\ ^2\Pi_{1/2} \leftarrow \widetilde{X}\ ^2\Pi_{1/2}$ transitions of HC$_4$S and DC$_4$S recorded with medium resolution (0.15 cm^{-1}) and high temperature (80 K) by means of DFWM. The $\widetilde{A}\ ^2\Pi_{1/2} \leftarrow \widetilde{X}\ ^2\Pi_{1/2}$ transitions of HC$_4$S and DC$_4$S were observed for the first time. Their analysis is presented in section 7.2.4.

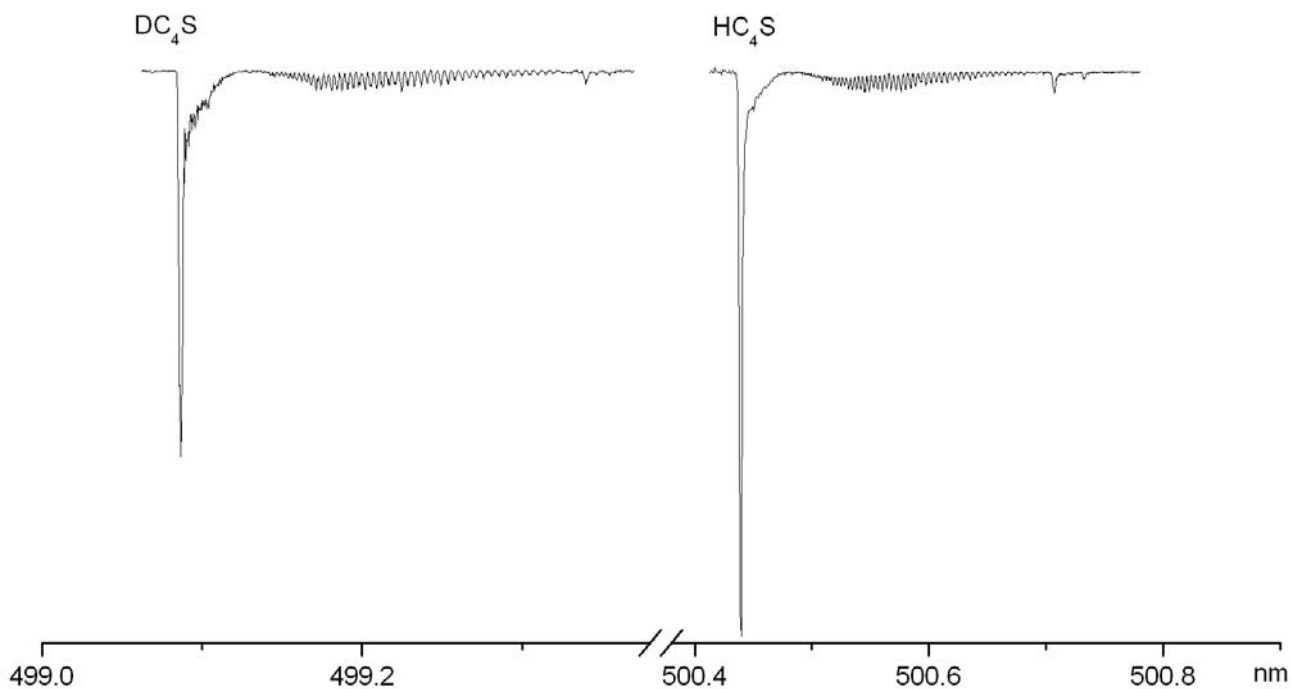**Figure 7.1. The $\widetilde{A}\ ^2\Pi_{3/2} \leftarrow \widetilde{X}\ ^2\Pi_{3/2}$ and $\widetilde{A}\ ^2\Pi_{1/2} \leftarrow \widetilde{X}\ ^2\Pi_{1/2}$ transitions of HC$_4$S and DC$_4$S measured by DFWM at 80K with 0.15 cm^{-1} resolution.**

7.2.1 Linewidth with laser power effects

Expressions (1.22) and (1.24) can be used to calculate the linewidth of the FWM signal. Considering the case in which $I << I_{sat}$, the denominator in Equation (1.22) is nearly equal to one and one obtains a cubed Lorentzian frequency dependency for the FWM signal in which the linewidth is nearly half that of the Lorentzian line. To include the linewidth of the laser, Equation (1.22) has to be convoluted with the laser spectrum for all frequencies. By assuming a Gaussian laser spectral power of full width at half maximum of 0.15 cm^{-1} and in the case where the natural linewidth of the transition is negligible, this results in a cubed Gaussian, which is also a Gaussian with width of 0.086 cm^{-1}, this of course provided that we are in the unsaturated regime of DFWM. For HC$_4$S, the Doppler linewidth is equal to 0.016 cm^{-1} at 100 K, which has also to be accounted for and resulting in a Gaussian lineshape of full width at half maximum equal to 0.087 cm^{-1}, which is smaller than our actual laser linewidth.

7.2.2 Comparison between CRDS and DFWM on HC$_4$S

The CRDS and DFWM spectra of the origin band of HC$_4$S are shown in Figure 7.2. Both spectra were measured at high/low temperature using an intracavity etalon installed in the dye laser, reducing the laser bandwidth down to ~ 0.04 cm^{-1}.
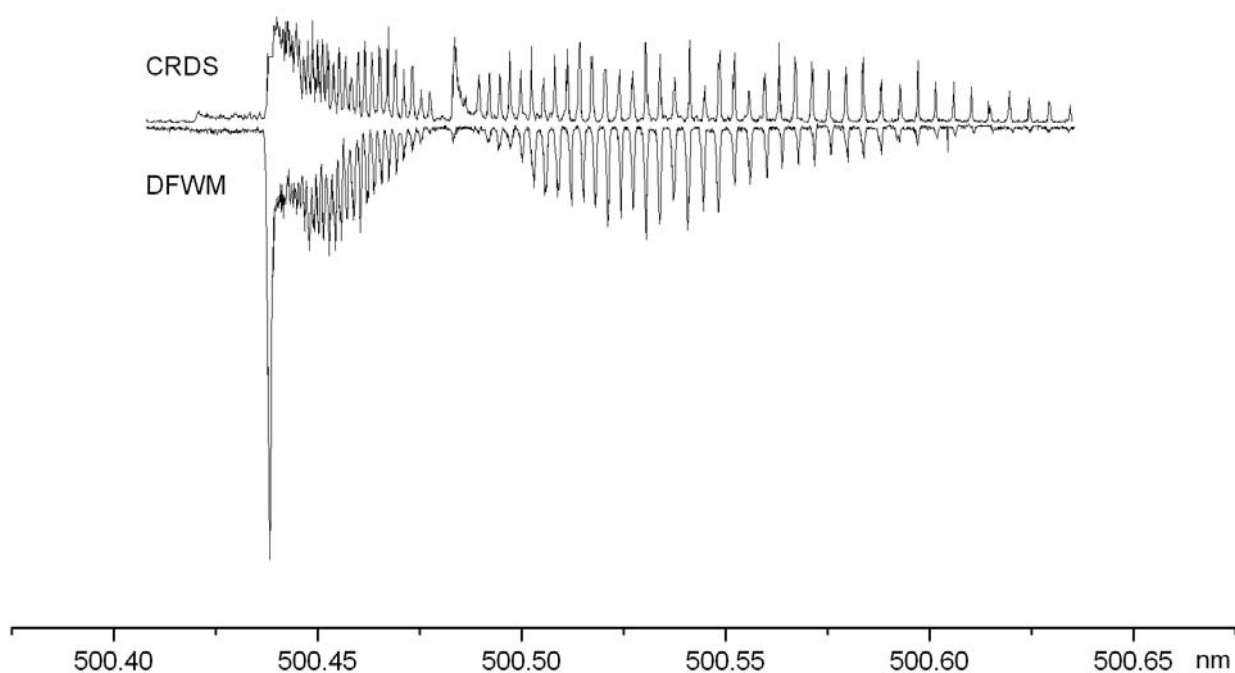
Figure 7.2. High resolution spectrum of the $\widetilde{A}\ ^2\Pi_{3/2} \leftarrow \widetilde{X}\ ^2\Pi_{3/2}$ **transitions of HC$_4$S radical obtained by CRDS (upper trace) and DFWM (lower trace). See text for the details.**

From the Equation (1.22) for the low energy regime, i.e. I $\ll$ I$_{sat}$, the signal wave intensity is cubic dependent on the input laser intensity. Because the incident beams have near Gaussian profile it follows:

$$I_s(\omega) \propto I^3(\omega) \propto e^{3\left(\frac{\omega-\omega_0}{\omega_d}\right)^2}$$

where ω_0 is the frequency in the center of the laser peak and ω_d is related to the FWHM of the peak according to $\mathrm{FWHM} = 2\sqrt{\ln 2}\,\omega_d$

Taking into account the effect of the finite laser bandwidth by integrating overall possible frequency

$$\text{linewidth of the signal wave} \propto \int\limits_{\substack{linewidth \\ of\ the\ laser}} I_s(\omega)d\omega \propto \int e^{3\left(\frac{\omega-\omega_0}{\omega_d}\right)^2} d\omega \propto \frac{\text{linewidth of the input wave}}{\sqrt{3}}$$

Thus the spectral resolution can be significantly improved in the DFWM experiments, allowing complex spectra consisting of closely spaced transitions to be more easily analyzed.

However, as discussed above, one prefers to work in near-saturated conditions, where the intensity of the signal beam reaches its maximum value. Here, laser fluctuations are not influence the signal. Because the cubic dependence on the incident radiation is no longer valid. The increase in resolution afforded by DFWM is accompanied by a decrease in sensitivity, because only a small number of molecules can participate in the nonlinear process, which furthermore has a quadratic dependence on the number density.

A great disadvantage of the CRDS technique is the saturation of strongly absorbing transitions in the line center (see Figure 7.3). Although this is not a general limitation of the technique, because it could be solved by reducing the absorption length, this fact prevents one from easily collecting overview spectra of the molecules of interest. Moreover, time resolution is limited by the ring-down time to at least 10 µs in this work.
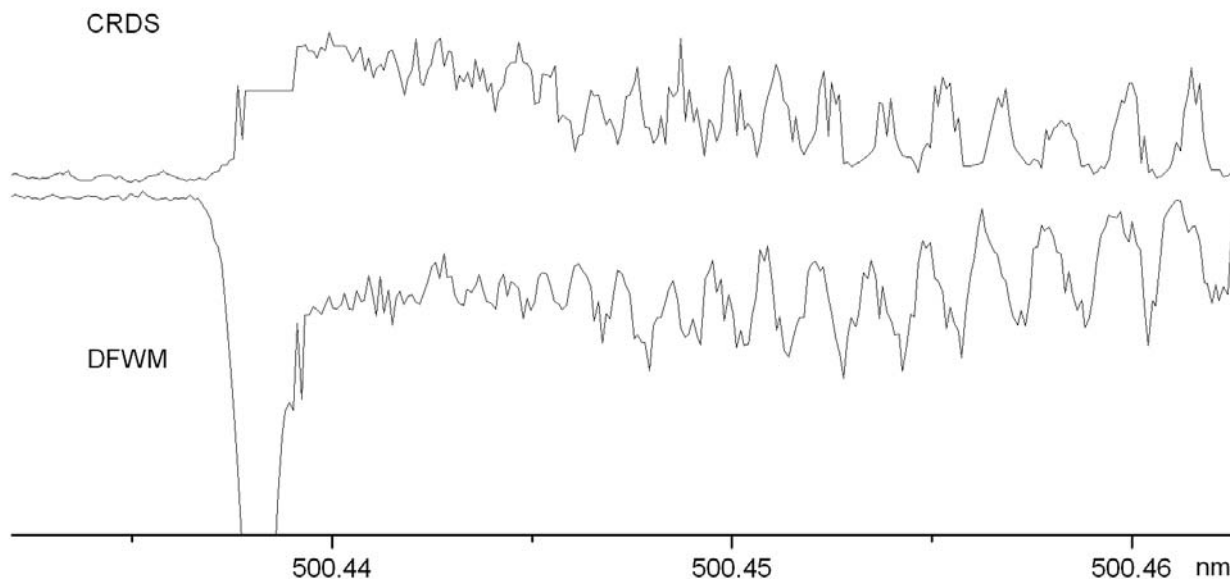
Figure 7.3. Saturation of strongly absorbing HC$_4$S transition in the CRDS experiment.

The reported sensitivities for DFWM fall in the range of 10^9 - 10^{12} molecules cm^3 per quantum state [22, 23, 120, 121], depending on the oscillator strength of the transitions involved and the extent of saturation.

Williams et al. [122] published an essay on the theoretical line strength based on diagrammatic perturbation theory where they showed that in the most general case the DFWM signal arises from the contributions of 12 different gratings. These gratings are distinguished by spacing by the level in which the grating is formed (ground and excited). In the forward-box configuration used in this work these gratings have the same spacing that can be calculated from the Equation (1.17) for $\lambda = 500$nm

$$d = \frac{0.5}{2\sin\frac{2}{2}} \approx 14.7\,\mu m$$

73

7.2.3 High resolution spectrum of HC$_4$S

In Figure 7.4 the rotationally resolved well-structured $\widetilde{A}\ ^2\Pi_{3/2} \leftarrow \widetilde{X}\ ^2\Pi_{3/2}$ transitions of HC$_4$S and its simulation are shown.
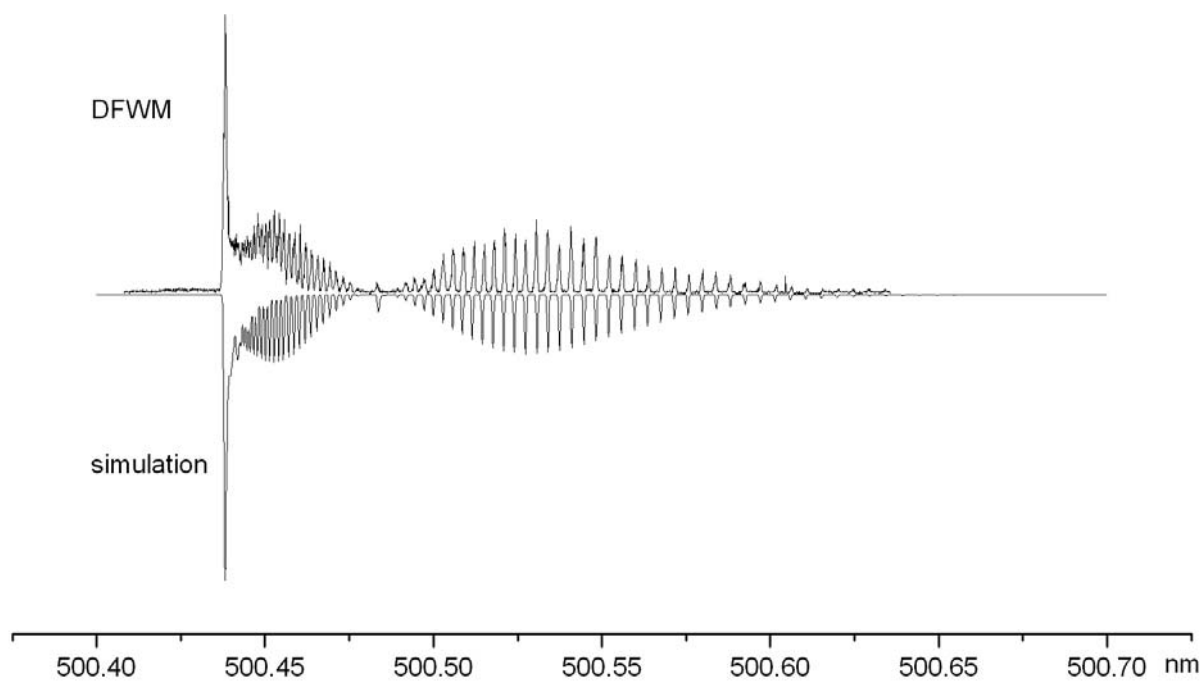
Figure 7.4. High-resolution DFWM spectrum of the $\widetilde{A}\ ^2\Pi_{3/2} \leftarrow \widetilde{X}\ ^2\Pi_{3/2}$ **origin band of the HC$_4$S radical and the simulation at 30K.**

The simulation has been performed using PGOPHER [123] and the constants obtained from a previous LIF experiment [116].

7.2.4 Spin-orbit constants of HC$_4$S

In Figure 7.5 the rotationally resolved $\Omega = \frac{3}{2}$ and $\Omega = \frac{1}{2}$ spin-orbit components of the

$\tilde{A}\ ^2\Pi \leftarrow \tilde{X}\ ^2\Pi$ origin band of the HC$_4$S measured by CRDS are shown.

a)
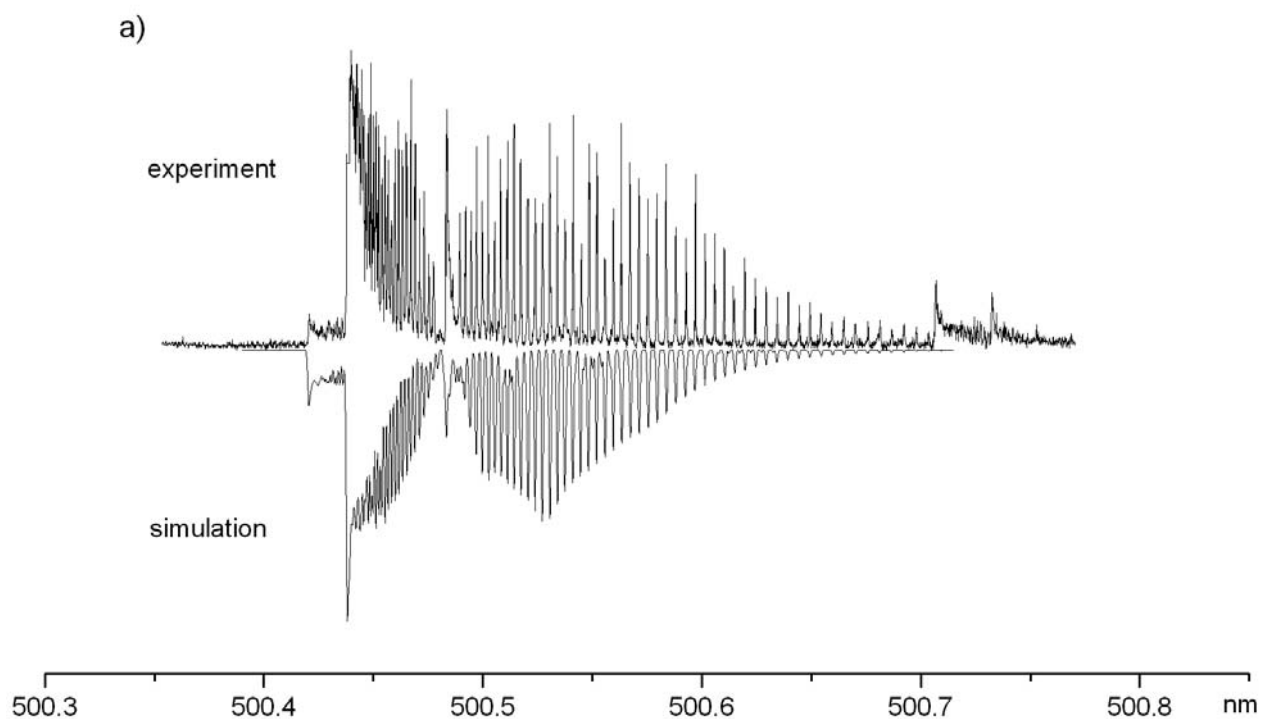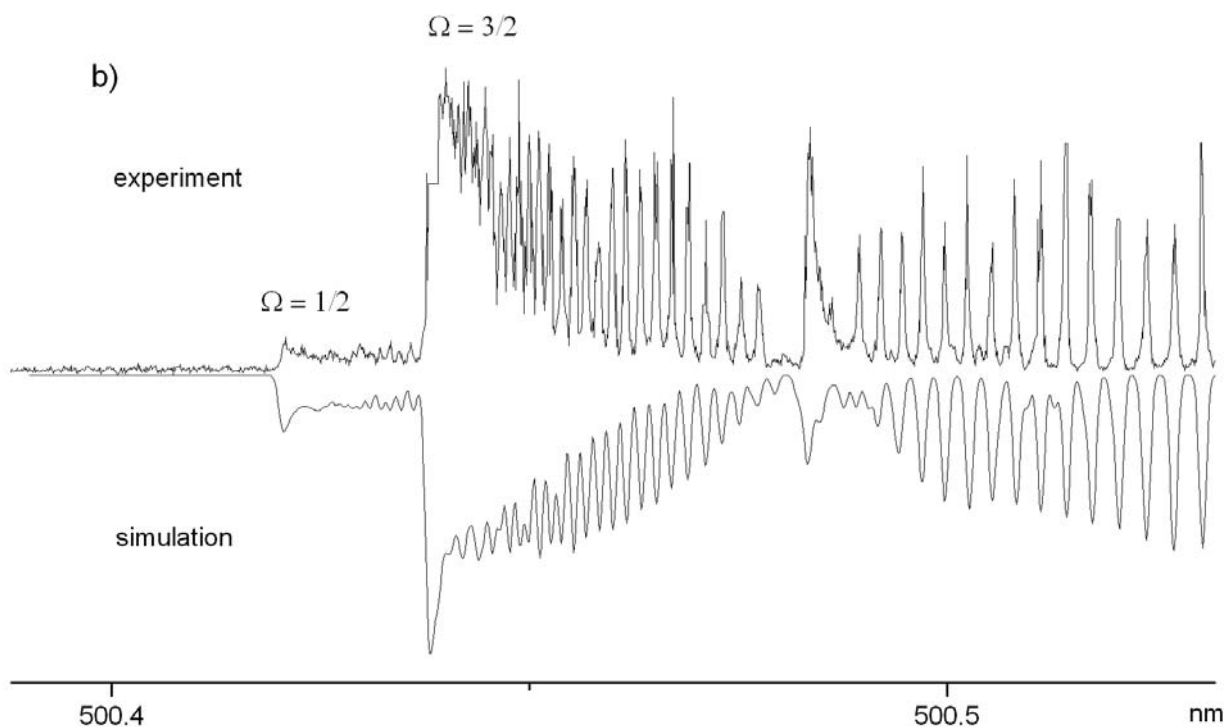
Figure 7.5. The two spin-orbit components in the origin band of the $\tilde{A}\ ^2\Pi \leftarrow \tilde{X}\ ^2\Pi$ electronic transition of HC$_4$S measured by CRDS. Some additional features are seen in a) (see text for the details). b) extended perspective. The rotational temperature was found to be 30 K.

The spin-orbit transition $\tilde{A}\ ^2\Pi_{1/2} \leftarrow \tilde{X}\ ^2\Pi_{1/2}$ of HC$_4$S was observed for the first time. However the spin-orbit components overlap as the difference in the spin-orbit splitting in the ground and excited state, ΔA, appears to be small. Thus, only 4 lines of $\tilde{A}\ ^2\Pi_{1/2} \leftarrow \tilde{X}\ ^2\Pi_{1/2}$ R- branch could be assigned. For the higher component ($\Omega = \frac{3}{2}$) 52 transitions in P – branch and 17 lines of the R – branch were identified with J – values up to 54.5. These values were then fitted with PGOPHER. Initially the rotational constants B″ and B′ were fixed to the values obtained in [116]. The spin-orbit interaction constant of the ground state, A″ of HC$_4$S was estimated to be ~-33 cm^{-1} [124]. The minus sign indicates that the $\Omega = \frac{3}{2}$ component is lower in energy than the $\Omega = \frac{1}{2}$, as was also observed for the HC$_2$S [125]. The one of the excited state was assumed to be about –33.7 cm^{-1}. The line positions were fitted with PGOPHER using

76

T_{00}, B", B', A", A' as variables yielding a rms of 0.01cm^{-1}. The resulting constants are listed in Table 7.1 and are in good agreement with whose previously derived from the microwave [124] and LIF experiment [116]. The spin-orbit interaction coefficients were found to be -31.864(49) cm^{-1} and -32.575(49) cm^{-1} for the ground and excited state respectively. Thus, the variation of the spin-orbit interaction constants was determined to be – 0.6 cm^{-1}. More precise values will be obtained from the prospective two-color resonant four wave mixing experiments, which enable to selectively discriminate between blended spectral features. The line frequencies and their assignments are listed in Table 7.2.

Table 7.1. Spectroscopic constants for HC$_4$S (in cm^{-1}). Values in parentheses denote the standard deviations and apply to the last digits of the constants.

	This work	LIF[a]	microwave[b]
A"	-31.864(49)		-33[c]
A'	-32.575(49)		
ΔA	-0.06		
B"	0.047874(33)		0.047807(1)
B'	0.046634(35)	0.046580(4)	
T_{00}	19981.0511(13)	19980.687(1)	

[a] Ref [116].
[b] Ref [124].
[c] estimated value by [124].

In addition, some weaker spectral features of HC$_4$S and DC$_4$S were observed blue-shifted with respect to the origin band (see Figure 7.6). One assumed that these are vibronic transitions from one of the lowest bending modes of the molecule.
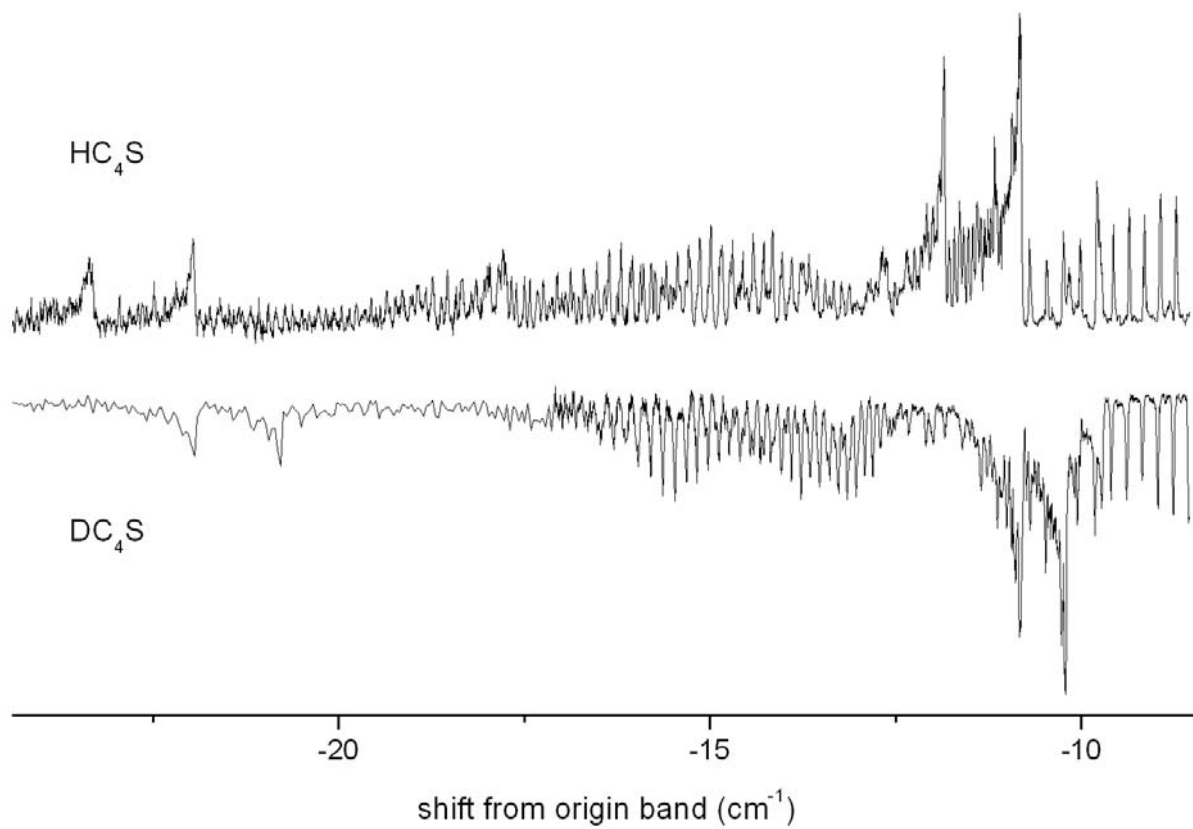
Figure 7.6. Presumed vibronic bands of HC$_4$S (upper trace) and DC$_4$S (lower trace). The spectra were measured by means of CRDS.

Table 7.2. Measured rotational frequencies of the $\tilde{A}\ ^2\Pi \leftarrow \tilde{X}\ ^2\Pi$ transition of HC$_4$S.

Transition J	ν_{obs} (cm^{-1})	o - c (cm^{-1})	ν_{obs} (cm^{-1})	o - c (cm^{-1})
$\Omega = \dfrac{3}{2}$	P - branch		R - branch	
1.5			19981.1158	-0.0183
2.5	19980.6368	-0.0183	19981.2013	-0.0214
3.5	19980.5318	-0.0214	19981.2882	-0.0185
4.5	19980.4303	-0.0185	19981.3696	-0.0085
5.5	19980.3334	-0.0085	19981.452	-0.0023
6.5	19980.2302	-0.0023	19981.5284	-0.0001
7.5	19980.1205	-0.0001	19981.608	-0.0024
8.5	19980.0039	-0.0024	19981.6809	0.0038
9.5	19979.8932	0.0038	19981.7515	0.0003
10.5	19979.7704	0.0003	19981.8157	0.0013
11.5	19979.6497	0.0013	19981.8814	0.0068
12.5	19979.5309	0.0068	19981.9428	0.0015
13.5	19979.3989	0.0015	19982.0009	-0.004
14.5	19979.2641	-0.0040	19982.0596	-0.0064
15.5	19979.1301	-0.0064	19982.1157	-0.0017
16.5	19979.0006	-0.0017	19982.1676	-0.0058
17.5	19978.8599	-0.0058	19982.2137	-0.0081
18.5	19978.7184	-0.0081	19982.2628	-0.014
19.5	19978.571	-0.0140		
20.5	19978.4238	-0.0171		

21.5	19978.281	-0.0134
22.5	19978.1335	-0.0119
23.5	19977.9913	-0.0026
24.5	19977.8387	-0.0013
25.5	19977.695	0.0115
26.5	19977.5356	0.0109
27.5	19977.3737	0.0104
28.5	19977.21	0.0105
29.5	19977.0438	0.0106
30.5	19976.8771	0.0126
31.5	19976.6986	0.0053
32.5	19976.5126	-0.0070
33.5	19976.3383	-0.0052
34.5	19976.1632	-0.0017
35.5	19975.9876	0.0037
36.5	19975.8157	0.0153
37.5	19975.6393	0.0248
38.5	19975.4417	0.0156
39.5	19975.2508	0.0156
40.5	19975.0523	0.0104
41.5	19974.8506	0.0044
42.5	19974.6492	0.0012
43.5	19974.4491	0.0018

44.5	19974.2529	0.0086
45.5	19974.0549	0.0162
46.5	19973.8556	0.0248
47.5	19973.639	0.0186
48.5	19973.4275	0.0200
49.5	19973.1975	0.0053
50.5	19972.9789	0.0044
51.5	19972.7588	0.0044
52.5	19972.5425	0.0107
53.5	19972.3139	0.0071
54.5	19972.093	0.0136

$\Omega = \dfrac{1}{2}$	P - branch		R - branch	
14.5			19982.7796	0.0135
15.5			19982.8339	0.0130
16.5			19982.8774	0.0042
17.5			19982.9281	0.0050

7.2.5 TC-FWM experiment on C_2

Two-color FWM is demonstrated on the several rovibrational transitions in the $d\,^3\Pi_g \rightarrow a\,^3\Pi_u$ Swan band of C_2. A spectrum (see Figure 7.7) was recorded by scanning the probe laser, when the pump beam was tuned to overlap with the $R_1(3)$ transition at 515.66 nm. As seen from the Figure 7.7 because only few TC-RFWM resonances that share the common ground and excited state appear, a dramatic simplification of the one-color spectra occurs. Furthermore, the transitions are restricted by the $\Delta J = 0, \pm 1$ selection rule. Therefore, congested spectra can be easily analyzed by using TC-RFWM. In Figure 7.7 2 SEP (stimulated emission pumping) and 2 UP (hole-burning) corresponding transitions were observed, one of each in the P and Q branches. The experimental linewidth of the lines is nearly twice the linewidth of the probe laser, indicating that spectra were measured in conditions above laser power saturation. In this case, chosen on purpose, the reproducibility in intensity of the spectral lines was improved. Figure 7.7-7.9 show several spectra recorded for different pump transitions close in frequency. They illustrate that such technique can be used to disentangle overlapping features, for example near the band head where many transitions are blended, by carefully selecting lines in the R branch. The emphasis should be drawn on the potential of two-color FWM compared to standard absorption techniques in analyzing complex molecular spectra.

Figure 7.7. TC-RFWM C$_2$ transitions in the $d\,{}^3\Pi_g \rightarrow a\,{}^3\Pi_u$ Swan band. The PUMP laser is fixed on the $R_1(3)$ line. 2 stimulated emission transitions and 2 transition from a transient grating produced from the depletion of the ground state by the PUMP laser are detected.

Figure 7.8. TC-RFWM C$_2$ transitions in the $d\ ^3\Pi_g \rightarrow a\ ^3\Pi_u$ Swan band. The PUMP laser is fixed on the $R_1(6)$ line. Strong allowed transitions are observed for $P_1(6)$ and $P_1(8)$ which are connected to the PUMP transition by the ground and excited state level, respectively.
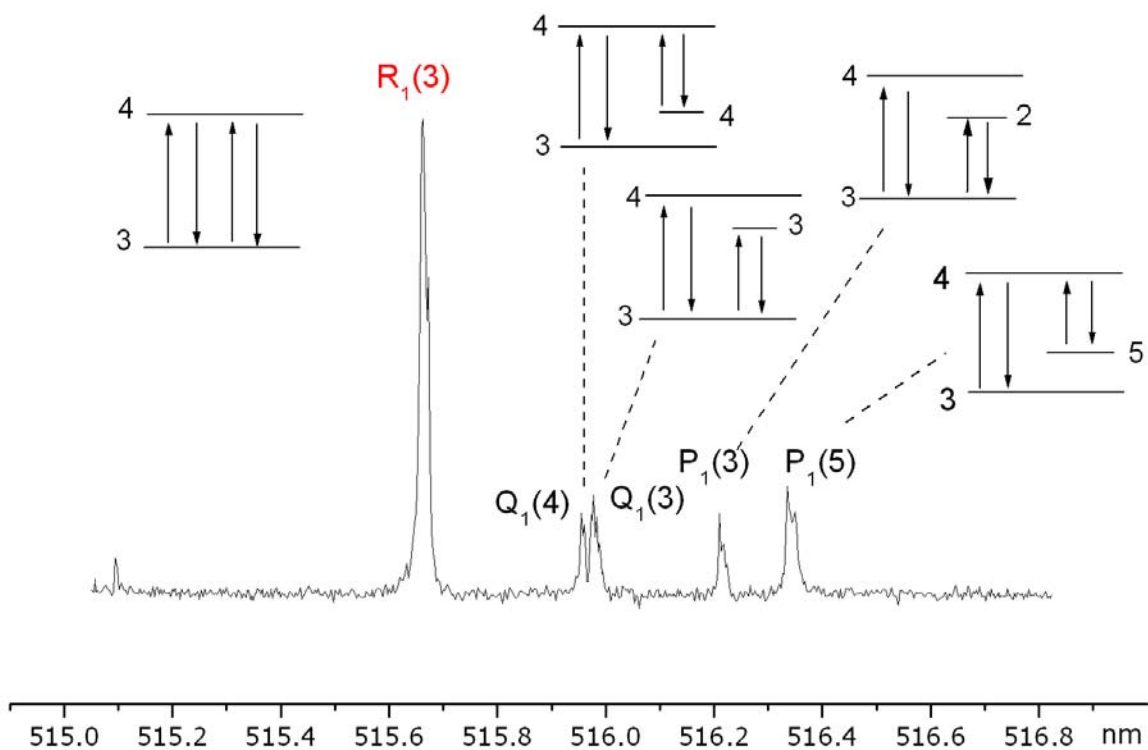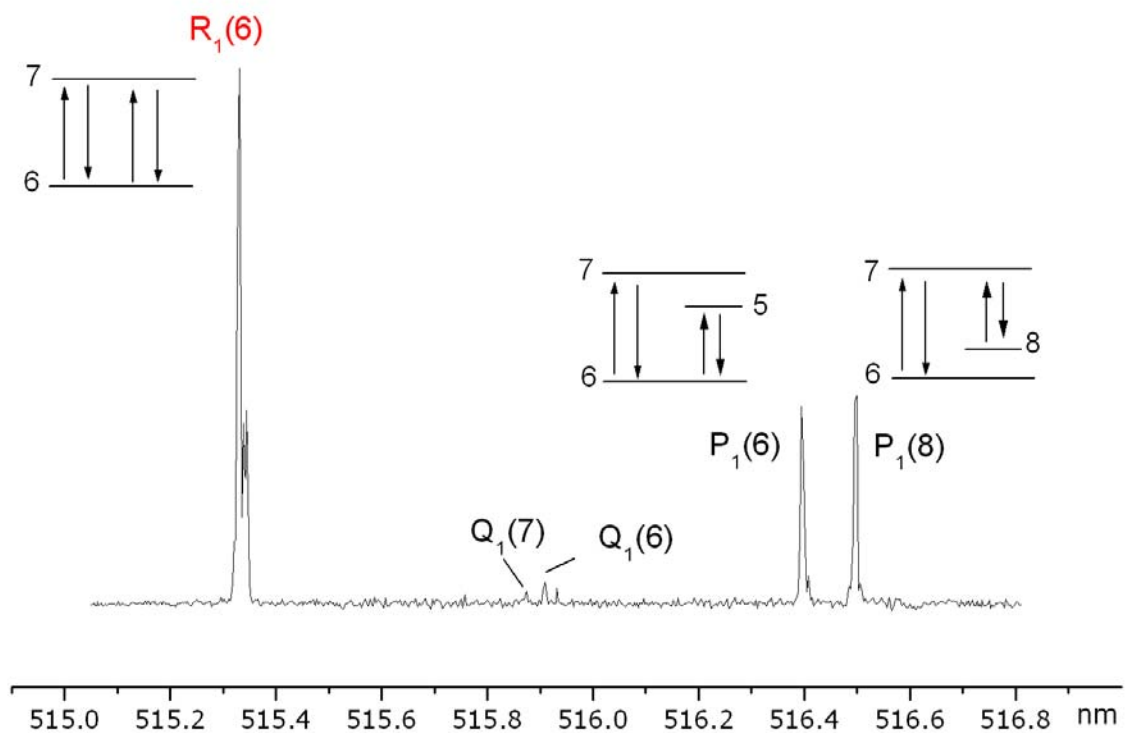
Figure 7.9. TC-RFWM C$_2$ transitions in the $d\,^3\Pi_g \rightarrow a\,^3\Pi_u$ Swan band. The PUMP laser is fixed on the $R_2(5)$ line. Strong allowed transitions are observed for $P_2(5)$ and $P_2(7)$ which are connected to the PUMP transition by the ground and excited state level, respectively.
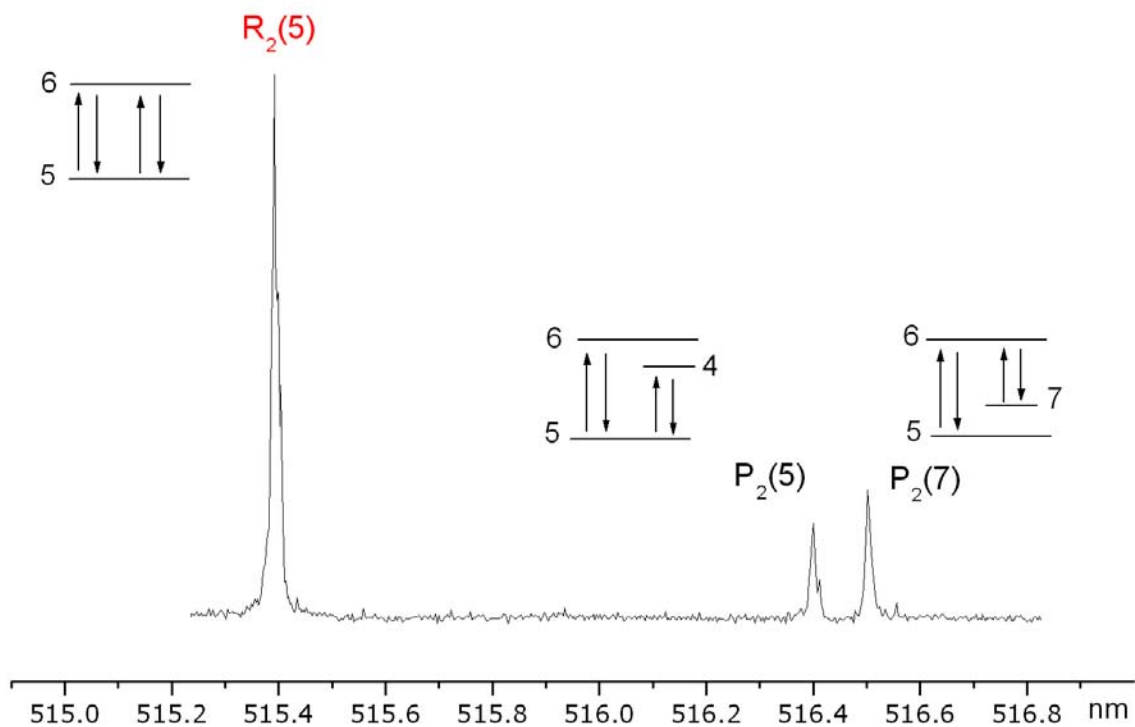
8 OUTLOOK

The first part of this work is devoted to spectroscopic studies of two radicals, C_3H_5 and C_3H_2, using cavity ring-down spectroscopy, a wildly used spectroscopic technique known for its high sensitivity and experimental simplicity. However, problems were encountered when measuring optical spectra: namely, the CRD spectrum of C_3H_5 was misassigned due to another absorber overlapping in the same spectral region. In the case of C_3H_2, the strong $\widetilde{B}$ ${}^1B_1$ - $\widetilde{X}$ ${}^1A_1$ transition could not be detected due to the short lifetime of the $\widetilde{B}$ state. Therefore a nonlinear optical probe (degenerate four wave mixing) was developed and combined with a slit nozzle source. The first experiments investigated C_2, which was previously studied using FWM technique only on high temperature (3000 K) oxy-acetylene flames. Direct comparison shows that while DFWM spectroscopy provides slightly less sensitivity (typically two or three orders of magnitude less then first order processes, such as CRDS), SN ratios are roughly 10 times greater. Moreover, spectra obtained by FWM are background free and very well structured. DFWM can also provide species selectivity, because the generated signal depends quadratically on concentration. After C_2 detection, C_3 was studied to improve the DFWM experimental setup and explore saturation effects.

Detection of HC_4S demonstrated that this technique is also applicable toward lager molecules, provided that one has synthesized sufficient concentrations. Thus, replacing a circular orifice with a slit nozzle increased the sample interaction length. This led to significant enhancement in the sensitivity. Reducing the cross angle between the three incident beams from 2º to under 1.5º lengthen the interaction path from 10-15 mm to 15-20 mm, also resulting in greater sensitivity.

Indeed, much of the interest in DFWM stems from its unique capabilities in situations where more conventional linear methods to fail. Thereby, one should be able to detect the strong $\widetilde{B}$ ${}^1B_1$ - $\widetilde{X}$ ${}^1A_1$ transition of C_3H_2, which has never been measured in the gas phase and is of high interest due to its astrophysical relevance.

Further improvements of the apparatus could involve rearranging the light paths. At the present stage, the experiments are performed with a forward box configuration. This has the advantage of easier signal extraction, however, it is not Doppler free. In contrast, a phase conjugate geometry, where two laser beams are directed through a molecular sample in a

coaxial and counterpropagating fashion, allows Doppler free response. However, because it emerges in a direction that is exactly collinear and counterpropagating with respect to the incident probe radiation, it requires additional optical devices for signal extraction. Once the phase-conjugate geometry is implemented, less sophisticated adjustment of the detection optics is required (i.e., when compared to the box schemes). The prospective scheme of such an experimental configuration is shown in Figure 8.1.
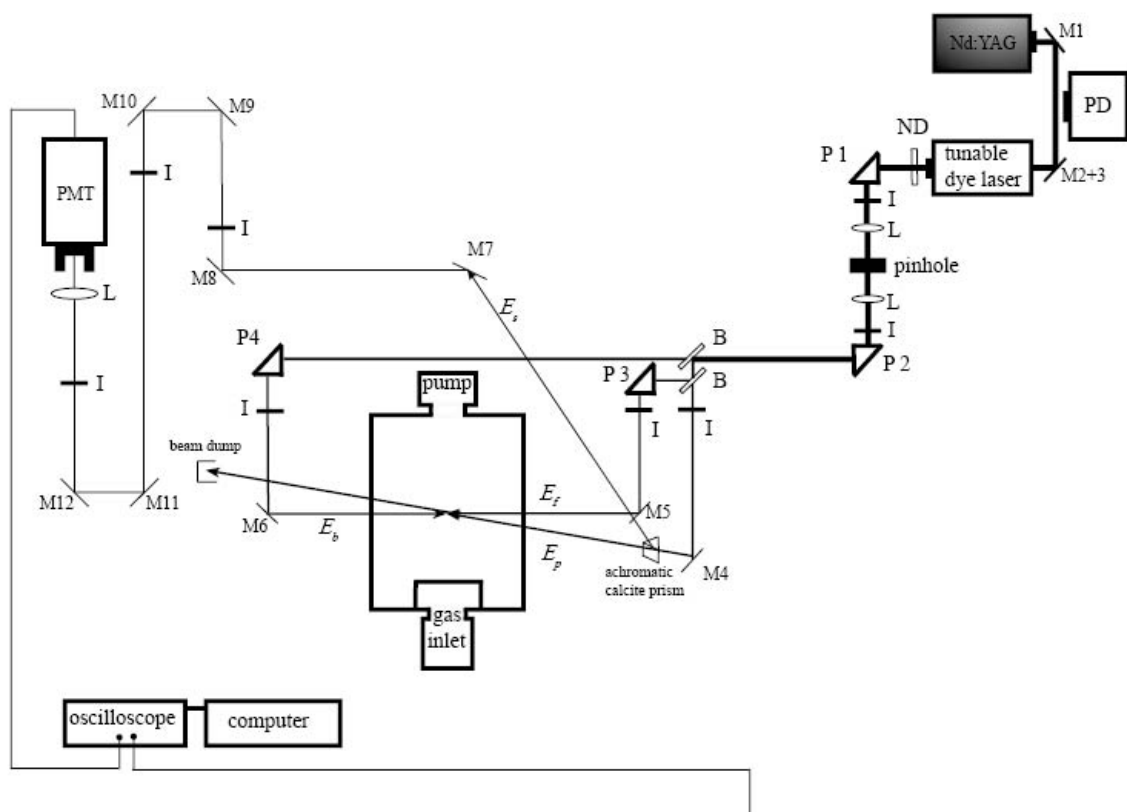
Figure 8.1. Experimental configuration for phase-conjugate DFWM spectroscopy. Three beams of identical frequency are directed into the vacuum chamber where they overlap with a supersonic free-jet expansion of target molecules. The forward-going pump (E_f) and probe (E_p) waves cross under a small angle, while the backward-going pump wave (E_b) is aligned to precisely retrace the path of E_f. The four-wave mixing signal (E_s), which emerges as a coherent beam that is coaxial and counterpropagating with respect to the incident probe radiation, can be isolated through the use of polarization-selective components (*e.g.* an achromatic calcite prism).

9 BIBLIOGRAPHY

1.   Hawarth, O., *Theory of spectroscopy*, 1973, New York: Halsted.

2.   R.D.L. Kronig, *Journal of the Optical Society of America and Review of Scientific Instruments*, 1926. 12(6): p. 547-557.

3.   S.S. Kano and M.D. Levenson, *Introduction to Nonlinear Laser Spectroscopy*, 1988, San Diego: Academic Press, Inc.

4.   A. Okeefe, and D.A.G. Deacon, *Review of Scientific Instruments*, 1988. 59(12): p. 2544-2551.

5.   D. Romanini and K.K. Lehmann, *Journal of Chemical Physics*, 1993. 99(9): p. 6287-6301.

6.   G. Meijer, M.G.H. Boogaarts, R.T. Jongma, D. H. Parker and A. M. Wodtke, *Chemical Physics Letters*, 1994. 217(1-2): p. 112-116.

7.   R.W. Boyd and G.P. Agrawal, *Contemporary Nonlinear Optics*, 1992, San Diego: Academic Press, Inc.

8.   M.S. Brown, L.A. Rahn and T. Dreier, *Optics Letters*, 1992. 17(1): p. 76-78.

9.   R.L. Farrow, D.J. Rakestraw and T. Dreier, *Journal of the Optical Society of America B-Optical Physics*, 1992. 9(10): p. 1770-1777.

10.   R.P. Lucht, R. Trebino and L.A. Rahn, *Physical Review A*, 1992. 45(11): p. 8209-8227.

11.   A.E. Bracamonte and P.H. Vaccaro, *Journal of Chemical Physics*, 2003. 119(2): p. 887-901.

12.   R.W. Field, E. Hirota, J.P. Maier and S. Tsuchiya, *Nonlinear Spectroscopy for Molecular Structure Determination.* 1998, Oxford: Blackwell Science Ltd.

13.   P. Günter, H.J. Eichler and D.W. Pohl, *Laser-Induced Dynamic Gratings*, 1986: Springer.

14.   H. Latzel, T. Dreier, M. Giorgi and R. Fantoni, *Berichte Der Bunsen-Gesellschaft-Physical Chemistry Chemical Physics*, 1997. 101(7): p. 1065-1070.

15.   A.E. Siegman, *Journal of the Optical Society of America*, 1977. 67(4): p. 545-550.

16.   A.C. Eckbreth, *Applied Physics Letters*, 1978. 32(7): p. 421-423.

17.   E.J. Friedmanhill, L.A. Rahn and R.L. Farrow, *Journal of Chemical Physics*, 1994. 100(6): p. 4065-4076.

18. P.M. Danehy, P.H. Paul and R.L. Farrow, *Journal of the Optical Society of America B-Optical Physics*, 1995. 12(9): p. 1564-1576.

19. R.L. Abrams and R.C. Lind, *Optics Letters*, 1978. 2(4): p. 94-96.

20. R.L. Abrams and R.C. Lind, *Optics Letters*, 1978. 3: p. 205-.

21. P. Ewart and S.V. Oleary, *Optics Letters*, 1986. 11(5): p. 279-281.

22. T. Dreier and D.J. Rakestraw, *Applied Physics B-Photophysics and Laser Chemistry*, 1990. 50(6): p. 479-485.

23. T. Dreier and D.J. Rakestraw, *Optics Letters*, 1990. 15(1): p. 72-74.

24. L.A. Rahn and M.S. Brown, Optics Letters, 1994. 19(16): p. 1249-1251.

25. E.F. McCormack, P.M. Dehmer, J.L. Dehmer and S.T. Pratt, *Journal of Chemical Physics*, 1995. 102(12): p. 4740-4746.

26. E.F. McCormack, S.T. Pratt, P.M. Dehmer and J.L. Dehmer, *Chemical Physics Letters*, 1993. 211(1): p. 147-155.

27. E.F. McCormack, S.T. Pratt, P.M. Dehmer, and J.L. Dehmer, *Chemical Physics Letters*, 1994. 227(6): p. 656-662.

28. N. Georgiev, U. Westblom and M. Alden, *Optics Communications*, 1992. 94(1-3): p. 99-102.

29. G. Meijer and D.W. Chandler, *Chemical Physics Letters*, 1992. 192(1): p. 1-4.

30. M. Versluis, G. Meijer and D.W. Chandler, *Applied Optics*, 1994. 33(15): p. 3289-3925.

31. I. Aben, W. Ubachs, P. Levelt, G. Vanderzwan and W. Hogervorst, *Physical Review A*, 1991. 44(9): p. 5881-5893.

32. N. Bohm and W. Kiefer, *Applied Spectroscopy*, 1993. 47(2): p. 246-247.

33. J. Gumbel and W. Kiefer, *Chemical Physics Letters*, 1992. 189(3): p. 231-235.

34. J. Gumbel and W. Kiefer, *Journal of the Optical Society of America B-Optical Physics*, 1992. 9(12): p. 2206-2209.

35. M.D. Wheeler, I.R. Lambert and M.N.R. Ashfold, *Chemical Physics Letters*, 1993. 211(4-5): p. 381-384.

36. M.D. Wheeler, I.R. Lambert and M.N.R. Ashfold, *Chemical Physics Letters*, 1994. 229(3): p. 285-290.

37. J.A. Gray, J.E.M. Goldsmith and R. Trebino, *Optics Letters*, 1993. 18(6): p. 444-446.

38.   D.S Green, T.G. Owano, S. Williams, D.G. Goodwin, R.N. Zare and C.H. Kruger, *Science*, 1993. 259(5102): p. 1726-1729.

39.   S. Williams, D.S. Green, S. Sethuraman and R.N. Zare, *Journal of the American Chemical Society*, 1992. 114(23): p. 9122-9130.

40.   T.A.W. Wasserman, A.A. Arias, T. Muller and P.H. Vaccaro, *Chemical Physics Letters*, 1996. 262(3-4): p. 329-336.

41.   A. Klamminger, M. Motzkus, S. Lochbrunner, G. Pichler, K.L. Kompa and P. Hering, *Applied Physics B-Lasers and Optics*, 1995. 61(3): p. 311-318.

42.   M. Motzkus, G. Pichler, M. Dillmann, K.L. Kompa and P. Hering, *Applied Physics B-Photophysics and Laser Chemistry*, 1993. 57(4): p. 261-265.

43.   G. Hall, A.G. Suits and B.J. Whitaker, *Chemical Physics Letters*, 1993. 203(2-3): p. 277-282.

44.   J.D. Tobiason, J.R. Dunlop and E.A. Rohlfing, *Journal of Chemical Physics*, 1995. 103(4): p. 1448-1469.

45.   T.J. Butenhoff and E.A. Rohlfing, *Journal of Chemical Physics*, 1993. 98(7): p. 5460-5468.

46.   B.A. Mann, S.V. Oleary, A.G. Astill and D.A. Greenhalgh, *Applied Physics B-Photophysics and Laser Chemistry*, 1992. 54(4): p. 271-277.

47.   B.A. Mann, R.F. White and R.J.S. Morrison, *Applied Optics*, 1996. 35(3): p. 475-481.

48.   A.P. Smith, G. Hall, B. J. Whitaker, A.G. Astill, D.W. Neyer and P.A. Delve, *Applied Physics B-Lasers and Optics*, 1995. 60(1): p. 11-18.

49.   M.A Buntine, D.W. Chandler and C.C. Hayden, *Journal of Chemical Physics*, 1992. 97(1): p. 707-710.

50.   T.J. Butenhoff and E.A. Rohlfing, *Journal of Chemical Physics*, 1992. 97(2): p. 1595-1598.

51.   S. Williams, J.D. Tobiason, J.R. Dunlop and E.A. Rohlfing, *Journal of Chemical Physics*, 1995. 102(21): p. 8342-8358.

52.   N. Georgiev and M. Alden, *Applied Physics B-Photophysics and Laser Chemistry*, 1993. 56(5): p. 281-286.

53.   V. Sick, M.N. Buipham and R.L. Farrow, *Optics Letters*, 1995. 20(19): p. 2036-2038.

54.   Q. Zhang, S.A. Kandel, T.A.W. Wasserman and P.H. Vaccaro, *Journal of Chemical Physics*, 1992. 96(2): p. 1640-1643.

55. P.P. Radi. and A.P. Kouzov, *Journal of Raman Spectroscopy*, 2002. 33(11-12): p. 925-933.

56. M. Tulej, M. Meisinger, G. Knopp, A.M. Walser, P. Beaud, T. Gerber and P.P. Radi, *Journal of Raman Spectroscopy*, 2006. 37(6): p. 680-688.

57. P. Derose, H.L. Dai and P.Y. Cheng, *Chemical Physics Letters*, 1994. 220(3-5): p. 207-213.

58. R.M. Helm, R. Neuhauser and H.J. Neusser, *Chemical Physics Letters*, 1996. 249(5-6): p. 365-372.

59. A.A Arias, T.A.W. Wasserman and P.H. Vaccaro, *Journal of Chemical Physics*, 1997. 107(14): p. 5617-5620.

60. G.J. Germann, R.L. Farrow and D.J. Rakestraw, *Journal of the Optical Society of America B-Optical Physics*, 1995. 12(1): p. 25-32.

61. Y. Tang and S.A. Reid, *Chemical Physics Letters*, 1996. 248(5-6): p. 476-481.

62. G.J. Germann and D.J. Rakestraw, *Science*, 1994. 264(5166): p. 1750-1753.

63. T. Muller and P.H. Vaccaro, *Chemical Physics Letters*, 1997. 266(5-6): p. 575-583.

64. H.Z. Li and W. Kong, *Journal of Chemical Physics*, 1998. 109(12): p. 4782-4790.

65. G. Hall and B.J. Whitaker, *Journal of the Chemical Society-Faraday Transactions*, 1994. 90(1): p. 1-16.

66. T.K. Ha, H. Baumann and J.F.M. Oth, *Journal of Chemical Physics*, 1986. 85(3): p. 1438-1442.

67. J.A. Blush, D.W. Minsek and P. Chen, *Journal of Physical Chemistry*, 1992. 96(25): p. 10150-10154.

68. J.D. DeSain, R.I. Thompson, S.D. Sharma and R.F. Curl, *Journal of Chemical Physics*, 1998. 109(18): p. 7803-7809.

69. E. Hirota, C. Yamada and M. Okunishi, *Journal of Chemical Physics*, 1992. 97(5): p. 2963-2970.

70. D. Uy, S. Davis and D.J. Nesbitt, *Journal of Chemical Physics*, 1998. 109(18): p. 7793-7802.

71. J.D. Getty, M.J. Burmeister, S.G. Westre and P.B. Kelly, *Journal of the American Chemical Society*, 1991. 113(3): p. 801-805.

72. G. Maier, H.P. Reisenauer, B. Rohde and K. Dehnicke, *Chemische Berichte-Recueil*, 1983. 116(2): p. 732-740.

73.   R. Engeln, *Paper presented at 51st Ohio State University Symposium on Molecular Spectroscopy*. 1996.

74.   C.L. Currie and D.A. Ramsay, *Journal of Chemical Physics*, 1966. 45(2): p. 488-&.

75.   K. Holtzhauer, C. Comettamorini and J.F.M. Oth, *Journal of Physical Organic Chemistry*, 1990. 3(4): p. 219-229.

76.   H.J. Deyerl, I. Fischer and P. Chen, *Journal of Chemical Physics*, 1999. 110(3): p. 1450-1462.

77.   H.J. Deyerl, T. Gilbert, I. Fischer and P. Chen, *Journal of Chemical Physics*, 1997. 107(8): p. 3329-3332.

78.   A.B. Callear and H.K. Lee, *Nature*, 1967. 213(5077): p. 693-&.

79.   A.D. Sappey and J.C. Weisshaar, *Journal of Physical Chemistry*, 1987. 91(14): p. 3731-3736.

80.   J.D. Getty, X.M. Liu and P.B. Kelly, *Journal of Physical Chemistry*, 1992. 96(25): p. 10155-10160.

81.   D.W. Minsek, J.A. Blush and P. Chen, *Journal of Physical Chemistry*, 1993. 97(33): p. 8674-8674.

82.   H.C. Longuethiggins and J.A. Pople, *Proceedings of the Physical Society of London Section A*, 1955. 68(7): p. 591-600.

83.   J.D. Getty, X.M. Liu and P.B. Kelly, *Chemical Physics Letters*, 1993. 201(1-4): p. 236-241.

84.   F.A. Houle and J.L. Beauchamp, *Journal of the American Chemical Society*, 1978. 100(11): p. 3290-3294.

85.   E. Achkasova, M. Araki, A. Denisov and J.P. Maier, *Molecular Physics*, 2005. 103(11-12): p. 1555-1560.

86.   E. Kim, M. Araki, R. Chauhan, P. Birza and J. P. Maier, *Molecular Physics*, 2006. 104(18): p. 2885-2890.

87.   K. Tonokura and M. Koshi, *Journal of Physical Chemistry A*, 2000. 104(37): p. 8456-8461.

88.   J.A. Miller, J.V. Volponi and J.F. Pauwels, *Combustion and Flame*, 1996. 105(4): p. 451-461.

89.   G. Maier, H. P. Reisenauer, W. Schwab, P. Carsky, B.A. Hess and L.J. Schaad, *Journal of the American Chemical Society*, 1987. 109(17): p. 5183-5188.

90.   A.M. Mebel, W.M. Jackson, A.H.H.Chang and S.H. Lin, *Journal of the American Chemical Society*, 1998. 120(23): p. 5751-5763.

91.   P. Thaddeus and M.C. McCarthy, *Spectrochimica Acta Part a-Molecular and Biomolecular Spectroscopy*, 2001. 57(4): p. 757-774.

92.   A.J. Apponi, M.C. MacCarthy, C.A. Gottlieb and P. Thaddeus, *Astrophysical Journal*, 2000. 530(1): p. 357-361.

93.   J.A. Hodges, R.J. McMahon, K.W. Sattelmeyer and J.F. Stanton, *Astrophysical Journal*, 2000. 544(2): p. 838-842.

94.   G. Herzberg and E. Teller, *Zeitschrift Fur Physikalische Chemie-Abteilung B-Chemie Der Elementarprozesse Aufbau Der Materie*, 1933. 21(5/6): p. 410-446.

95.   G. Herzberg, *Molecular Spectra and Molecular Structure*, 1967, Canada: D. Van Nostrad Company, Inc.

96.   J.A. Pople and J.W. Sidman, *Journal of Chemical Physics*, 1957. 27(6): p. 1270-1277.

97.   J.M. Vrtilek, C.A. Gottlieb, E.W.Gottlieb, T.C. Killian and P. Thaddeus, *Astrophysical Journal*, 1990. 364(2): p. L53-L56.

98.   P. Birza, A. Chirokolava, M. Araki, P. Kolek and J.P. Maier, *Journal of Molecular Spectroscopy*, 2005. 229(2): p. 276-282.

99.   C.A. Gottlieb, T.C. Killian, P. Thaddeus, P. Botschwina, J. Flugge and M. Oswald, *Journal of Chemical Physics*, 1993. 98(6): p. 4478-4485.

100.   A.S King and R.T. Birge, *Astrophysical Journal*, 1930. 72(1): p. 19-40.

101.   R. Mecke, *Physikalische Zeitschrift*, 1925. 26: p. 217-237.

102.   R.C. Johnson, *Philosophical Transactions of the Royal Society of London Series a-Containing Papers of a Mathematical or Physical Character*, 1927. 226: p. 157-U17.

103.   J.D. Shea, *Physical Review*, 1927. 30(6): p. 825-843.

104.   G. Herzberg, *Physical Review*, 1946. 70(9-10): p. 762-764.

105.   J.G. Phillips, *Astrophysical Journal*, 1948. 107(3): p. 389-&.

106.   R.S. Mulliken, *Physical Review*, 1927. 29(5): p. 0637-0649.

107.   R.S. Mulliken, *Physical Review*, 1929. 33(4): p. 0507-0511.

108.   R.C. Johnson and R.K. Asundi, *Proceedings of the Royal Society of London Series a-Containing Papers of a Mathematical and Physical Character*, 1929. 124(795): p. 668-688.

109. C.F. Kaminski, I.G. Hughes and P. Ewart, *Journal of Chemical Physics*, 1997. 106(13): p. 5324-5332.

110. K. Nyholm, M. Kaivola and C.G. Aminoff, *Optics Communications*, 1994. 107(5-6): p. 406-410.

111. K. Nyholm, M. Kaivola and C.G. Aminoff, *Applied Physics B-Lasers and Optics*, 1995. 60(1): p. 5-10.

112. M.B. Bell, L.W. Avery and P.A. Feldman, *Astrophysical Journal*, 1993. 417(1): p. L37-L40.

113. J. Cernicharo, M. Guelin, H. Hein and C. Kahane, *Astronomy and Astrophysics*, 1987. 181(1): p. L9-L12.

114. T.J. Millar, J.R. Flores and A.J. Markwick, *Monthly Notices of the Royal Astronomical Society*, 2001. 327(4): p. 1173-1177.

115. S.L. Krishnamachari and T.V. Venkitachalam, *Chemical Physics Letters*, 1978. 55(1): p. 116-118.

116. M. Nakajima, Y. Sumiyoshi and Y. Endo, *Chemical Physics Letters*, 2002. 351(5-6): p. 359-364.

117. M. Nakajima, Y. Sumiyoshi and Y. Endo, *Chemical Physics Letters*, 2002. 355(1-2): p. 116-122.

118. A. Denisov, T.W. Schmidt, A.E. Boguslavskiy, H. Ding, M. Araki and J.P. Maier, *International Journal of Mass Spectrometry*, 2004. 233(1-3): p. 131-136.

119. N.J. Reilly, G.C. Cupitt, S.H. Kable and T.W. Schmidt, *Journal of Chemical Physics*, 2006. 124(19): p. -.

120. S. Williams, E.A. Rohlfing, L.A. Rahn and R.N. Zare, *Journal of Chemical Physics*, 1997. 106(8): p. 3090-3102.

121. S. Williams, R.N. Zare and L.A. Rahn, *Journal of Chemical Physics*, 1994. 101(2): p. 1093-1107.

122. S. Williams, R.N. Zare and L.A. Rahn, *Journal of Chemical Physics*, 1994. 101(2): p. 1072-1092.

123. C.M. Western, *PGOPHER*. 1998, UK: School of Chemistry, University of Bristol.

124. Y. Hirahara, Y. Ohshima and Y. Endo, *Journal of Chemical Physics*, 1994. 101(9): p. 7342-7349.

125. J. Tang and S. Saito, *Journal of Chemical Physics*, 1996. 105(18): p. 8020-8033.

10 CURRICULUM VITAE

Personal information:

Name: Elena Achkasova

Day of birth: 11.07.1981

Place: Kamchatka, Russia

Nationality: Russian

Marital status: Single

Education:

1988 – 1998   Primary and secondary school No. 46, Petropavlovsk-Kamchatsky

1998 – 2002   Novosibirsk State University, Natural Sciences Department, Novosibirsk,
                Russia. B.Sc. in Environmental Chemistry.

2002 – 2003   University of Basel, Department of Chemistry, Switzerland, M.Sc. in
                Chemistry.

2002 – 2004   Novosibirsk State University, Natural Sciences Department, Novosibirsk,
                Russia. M.Sc. in Chemistry.

2003 – 2007   University of Basel, Department of Chemistry, Switzerland, Ph.D. work in the
                group of Prof. John. P. Maier